Electrode material–ionic liquid coupling for electrochemical energy storage

Xuehang Wang[1], Maryam Salari[2], De-en Jiang[3], Jennifer Chapman Varela[2] Babak Anasori[1], David J. Wesolowski[4], Sheng Dai[4], Mark W. Grinstaff[2] and Yury Gogotsi[1]

[1]*A.J. Drexel NanomaterialsInstitute and Department of Materials Science and Engineering, Drexel University, Philadelphia, PA, USA.*

[2]*Departments of BiomedicalEngineering and Chemistry,Boston University, Boston, MA, USA.*

[3]*Department of Chemistry,University of California, Riverside, CA, USA.*

[4]*Chemical Sciences Division,Oak Ridge National Laboratory, Oak Ridge, TN, USA.*

Abstract

The development of new electrolyte and electrode designs and compositions has led to advances in electrochemical energy-storage (EES) devices over the past decade. However, focusing on either the electrode or electrolyte separately is insufficient for developing safer and more efficient EES devices in various working environments, as the energy-storage ability is determined by the ion arrangement and charge and/or electron transfer at the electrode–electrolyte interface. In this Review, we assess the fundamental physicochemical and electrochemical properties at the electrode–electrolyte interfaces in Li-ion batteries and supercapacitors using safe and electrochemically stable ionic-liquid electrolytes. Key reactions and interactions at the electrode– electrolyte interface, as well as geometric constraints and temperature effects, are highlighted. Building on the fundamental understanding of interfacial processes, we suggest potential strategies for designing stable and efficient ionic-liquid-based EES devices with emerging electrode materials.

Acknowledgements

This research was sponsored, in part, by the Fluid Interface Reactions, Structures and Transport (FIRST) Center, an Energy Frontier Research Center funded by the US Department of Energy, Office of Science and Office of Basic Energy Sciences. The work of M.S., J.C.V. and M.W.G. at Boston University was supported by Samsung Electronics Co. (Samsung Advanced Institute of Technology, SAIT). The authors also acknowledge K. Van Aken, A. Levitt and X. Lin for helpful discussions.

This is the author's manuscript of the article published in final edited form as:

Wang, X., Salari, M., Jiang, D., Chapman Varela, J., Anasori, B., Wesolowski, D. J., Dai, S., Grinstaff, M. W., & Gogotsi, Y. (2020). Electrode material–ionic liquid coupling for electrochemical energy storage. Nature Reviews Materials, 5(11), 787–808. https://doi.org/10.1038/s41578-020-0218-9

The demand for portable electric devices, electric vehi- cles and stationary energy storage for the electricity grid is driving developments in electrochemical energy-storage (EES) devices[1,2]. Significant efforts are dedicated to increasing the energy-storage capacity of EES devices while simultaneously providing greater charge–discharge rates, improved safety and longer cycling stability to satisfy the ever-growing industrial and consumer demands. Attention is particularly focused on the market-dominant Li-ion batteries (LIBs) and supercapacitors used in automotive, mining, solar and wind energy, oil industry, military and aero- space electronics applications. These applications require EES devices to operate safely and efficiently in different environments, especially at high and low temperatures[3] (300 to −100 °C; Fig. 1a). Accelerated side reactions at elevated temperatures lead to cell failure, resulting in poor cycling performance and safety issues, whereas high ion-transport resistance and low reaction rates at low temperatures greatly reduce the energy and power density of devices.

The electrolyte is an essential component in EES devices, as the electrochemical energy-storage process occurs at the electrode–electrolyte interface, and the electrolyte acts as a bridge to transport ions between the positive and negative electrodes. To develop efficient EES devices, it is crucial to maximize the oxidation and reduction resistance of electrolytes on the electrodes by optimizing the activation energy of the electrochemical reactions and overpotential, while achieving sufficient ion transport. LIBs typically use an electrolyte developed in the 1990s composed of 1 M lithium hexafluorophosphate ($Li[PF_6]$) in ethylene carbonate (EC) and a linear carbonate ester. Carbonate-based organic electrolytes decompose and form a Li^+-conductive solid electrolyte interphase (SEI) layer on the graphite anode, preventing solvent co-intercalation and enabling stable operation of the battery within a 4-V window. Conventional supercapacitors use an organic electrolyte, comprising ammonium cations and fluorinated anions, in acetonitrile (ACN), affording a relatively narrow operating voltage window of <2.7 V and does not break down to form an SEI layer. However, conventional organic electrolytes barely meet the requirement for safe and efficient operation over a wide temperature range. Conventional electrolytes fail at elevated temperatures for several reasons: electrolytes based on organic solvents are highly volatile and flammable; the SEI layer decomposes above 70 °C, leading to continuous decomposition of the electrolyte and device failure; and the $Li[PF_6]$ used in LIBs degrades at temperatures above 55 °C, forming corrosive components, such as strong Lewis acids (for example, PF_5) and hydrofluoric acid. Although narrowing the voltage window and increasing the operating rate can mitigate some side reactions to prolong the cycling life at high temperature, it also considerably lowers the energy-storage capability. At low temperatures, the ionic conductivity of organic electrolytes decreases significantly to only a few mS cm^{-1}, increasing the ion-transport resistance and, consequently, decreasing the capacity[4]. In addition, the rate of the electrochemical reactions decreases and the charge-transfer resistance increases dramatically when the temperature decreases, which significantly decreases the energy and power density of devices.

Ionic liquids (ILs), composed entirely of positive (cation) and negative (anion) charge carriers, are a promising and safe alternative to conventional organic electrolytes, owing to their high electrochemical stability, high thermal stability, negligible vapour pressure and non-flammability[5,6] (Fig. 1b). Compared with organic and aqueous electrolytes, ILs exhibit superior electrochemical stability, enabling IL-based EES devices to stably operate within a wide electrochemical potential window of, in some cases, up to 6 V, which in turn provides a higher energy density[7]. To control the physicochemical and electrochemical properties, ILs can be mixed to form eutectic phases, or the cations and anions can be designed to have different asymmetries or altered ionic interactions. Diverse emerging energy-storage technologies are benefiting from the unique properties of ILs. The high solubility of ILs in polymers allows for the application of ILs in gel electrolytes with good ionic

conductivity. Moreover, IL-based gels are promising and safe electrolytes for the textile industry, owing to their non-volatility and non-flammability, as evaporation of the electrolyte leads to the decay of energy efficiency and capacity[8]. Additionally, lithium polysulfides are poorly soluble in ILs, enhancing the cycling stability of Li–S batteries[9]. The potential of ILs to operate under extreme environments was showcased when an IL-based LIB was selected as the power source for a microsatellite launched in 2014 (reF.10).

The widespread use of ILs in conventional EES devices is currently limited, as the energy and power density of IL-based EES devices are insufficient to compensate for the high costs of the IL. The advantageous electrochemical stability of ILs does not always yield a wider electrochemical stability window (ESW) and greater energy density in an EES device because of irreversible interfacial reactions at the electrodes, especially at high temperatures. The moderately high ion-transport resistance of ILs, especially under confinement and at low temperatures, also lowers the high-rate performance of IL-based EES devices. To spur interest in IL electrolytes for next-generation EES devices, it is crucial to have a comprehensive understanding of the interactions and reactions at the IL–electrode interface (Fig. 1c). In this Review, we focus on the structure of the IL–electrode interface, the interfacial electrochemical reactions, the ion-transport dynamics under confinement and the effects of extreme temperatures to reveal the impact of electrode and electrolyte coupling on the performance of LIBs and supercapacitors.

Thermally stable and efficient ILs

The intrinsic properties of ILs are determined by the chemical structure and electrostatic interactions of its constituent ions. ILs are generally divided into three classes according to the composition of the cation: aprotic, protic or metal-containing[11] (Fig. 2a,b). Aprotic and protic ILs share similar properties, but protic cations have a labile proton. The cation of a metal-containing IL is a metal-ion-containing complex[12], such as a Li-crown ether[13] or Li–glyme[14]. The emergence of metal containing ILs meets the need for a system that requires a metallic ionic environment with a liquid phase. To achieve safe and efficient operation of EES devices over a wide temperature window, high thermal stability and good ionic conductivity are required from the electrolyte.

Design for high thermal stability

For effective operation of EES devices at elevated temperatures, the electrolyte must be thermally stable to avoid decomposition and high vapour pressure, either of which can destroy the device. ILs generally exhibit high thermal stability, extending to temperatures above 300°C. The thermal stability of ILs is strongly correlated with the cation type. Pyrrolidinium ILs are generally more heat-resistant than imidazolium, pyridinium and non-cyclic tetraalkylammonium cations. For example, 1-butyl-1-methyl-pyrrolidinium bis(trifluoromethanesulfonyl)imide ([PYR14][TFSI]), one of the most commonly used nitrogen-based IL electrolytes, is thermally stable up to 350–380°C. Among the ILs with saturated cyclic ammonium cations, pyrrolidinium ILs also demonstrate greater thermal stability than their piperidinium and morpholinium analogues[15], although one piperidinium IL (N-methyl-N-methoxyethoxyethyl-piperidinium bis(trifluoromethanesulfonyl)imide) has demonstrated a high decomposition temperature of 356°C (reF.[16]). The less studied phosphonium-based ILs also show good thermal stability. For example, the decomposition temperature of [(C6)3PC10][TFSI] (where [(C6)3PC10]+ is decyl(trihexyl)phosphonium) is 355°C, and, when used as an electrolyte with Li[TFSI] in a battery, cells operated for 30 days at 100°C (reF.[17]). By contrast, sulfonium ILs are less thermally stable than their corresponding nitrogen-based ILs. Additionally, the number of nitro-

gen, phosphorus or sulfur atoms in the cation, the types of substituents on the heteroatom, the chain length of substituents and the hydrophobicity of the anion all influence the thermal stability of ILs; for more information, see reF.[15].

The decomposition temperature of Li-based salts, which provide the Li ions in the electrolyte for LIBs, is dependent on the composition of the anion. Li[TFSI] has a decomposition temperature of 384°C, which is higher than that of lithium bis(oxalato)borate (Li[BOB], ~300°C), lithium (fluorosulfonyl)(trifluoromethanesulfonyl)imide (Li[FTI], ~300°C) and lithium bis(fluorosulfonyl)imide (Li[FSI], 70°C)18. Commercial devices primarily use Li[PF6] because of its high solubility in organic solvents and ionic conductivity. However, the operation of LIBs at elevated temperatures (~55°C) expedites [PF6]− degradation. Although replacing [PF6]− with [TFSI]− or [BOB]− has been evaluated, [PF6]− remains unrivalled for practical applications. New Li salts must meet or exceed the performance of Li[PF6], including the formation of a uniform SEI layer on the electrodes; Li+ migration and high solubility in a wide range of nonaqueous solvents; compatibility with Al current collectors to avoid anodic dissolution; and chemical, thermal and electrochemical stability.

Design for high ionic conductivity

Many ILs suffer from a moderately high viscosity, high melting point and low ionic conductivity near the melting point, which diminishes EES device performance at low temperatures and high operating rates. Coulombic and van der Waals interactions (London dispersion, dipole–dipole and hydrogen bonding) between the cations and anions, as well as the molecular weight and structure of the ions, affect the viscosity. Generally, using larger ions, lengthening the alkyl chains or decreasing the charge on the ions decreases the viscosity of ILs, owing to the reduced activation energy for the ions to flow past one another[19]. IL viscosity decreases with temperature following the Arrhenius equation, except near the glass-transition temperature[20]. The ionic conductivity of ILs is also directly related to the temperature, with decreased conductivity at lower temperatures, owing to the presence of fewer free ions[21].

The present focus is on reducing ion pairing to impart sufficient fluidity and, hence, increase the mobility of the ions in IL electrolytes at ambient and sub-ambient temperatures. One common approach is to mix the IL with a low-viscosity organic solvent such as EC, ACN, propylene carbonate (PC), dimethyl carbonate (DMC), diethyl carbonate (DEC) or ethylmethyl carbonate[22]. The polar aprotic solvents solvate charged species owing to their large dipole moments. Among these solvents, IL mixtures with ACN achieve the most efficient ion transport and highest conductivities (tens of mS cm−1). However, the high volatility, flammability and toxicity due to the low flash point of ACN (~5 °C) and formation of [CN]− and NOx as combustion products, raises health and environmental concerns and renders ACN impractical for high-temperature applications[23]. Some carbonate-based solvents, especially glycerol-carbonate-based electrolytes, are environmentally compatible (that is, biodegradable, renewable or recyclable) and safe at high temperatures, but the ionic conductivity is relatively low[24].

The molecular size and weight of the organic solvents are crucial factors in determining the solvent–solute interactions and controlling the ionic conductivity of the liquid, whereas there is less correlation between the dielectric constant of the solvent and ion trans- port. Molecular dynamics (MD) simulations reveal that the diffusivity of the pure organic solvent, rather than the solvent polarity or the molecular weight, is the key to achieving good ion diffusivity in mixtures of ILs with different polar organic solvents[25]. However, solvating the charged species also decreases the

electrochemical stability and compromises the thermal stability and flammability of the electrolyte[26]. Note that IL–solvent electrolytes are sometimes incorrectly referred to as ILs. Upon addition of solvent, the IL acts as a salt in an organic electrolyte or, if only a small amount of solvent is added, a solvent-in-salt electrolyte forms.

An alternative approach to reduce the viscosity and melting point is to mix two ILs with different cations. Analysis of the diffusion coefficients of anions and cations revealed that the solidification process is largely independent of the anions, whereas cations have a role in preventing anion ordering[27–29]. For example, addition of 10 mol% [BenzMIM][TFSI] to [EMIM][TFSI] (where [BenzMIM]+ is 1-benzyl-3-methylimidazolium and [EMIM]+ is 1-ethyl-3-methylimidazolium) leads to a lower viscosity and an ionic conductivity that is ~22% higher than that of neat [EMIM][TFSI] at 50 °C (reF.30). Binary mixtures of ILs have also been investigated in order to shift the crystallization to lower temperatures[4,31]. For example, a eutectic mixture forms when 1-butyl- 4-methylpyridinium tetrafluoroborate ([BMP][BF4]) and 1-butyl-3-methylimidazolium tetrafluoroborate ([BMIM][BF4]) are mixed[32]. On the basis of the melting temperatures of various mixtures, determined by differential scanning calorimetry, the phase diagram in Fig. 2c was proposed[32]. The dimensional mismatch between the cations inhibits the anion arrangement and, thus, lowers the melting temperature of the eutectic mixture. The partial solubility of ILs in each other should also be investigated using differential scanning calorimetry as a function of various molar fractions. Collecting additional data near the eutectic points is warranted to more accurately establish the phase behaviour in this region and, thus, the mutual solubility of two ILs.

Confining an IL alters the melting point. For example, bulk [BMIM][PF6] has a melting point of 6 °C; however, the melting point increases to >200 °C when confined within multi-walled carbon nanotubes[33]. By contrast, the melting point of many ILs (including [BMIM][TFSI], [BMIM][FSI], [BMIM][PF6] and [EMIM][PF6]) is suppressed when they are confined in glass, and the melting point decreases linearly with the inverse of the pore size[34]. According to the Radhakrishnan–Gubbins corresponding states theory of fluid–solid phase transitions in slit pores, the shift in the melting point of the confined electrolyte relative to that of the bulk electrolyte is determined by the slit pore width and a dimensionless parameter α (where α = strength of wall–fluid attraction/ strength of fluid–fluid attraction)[35]. Therefore, confinement can either increase or decrease the melting (or freezing) point of the electrolyte: if $\alpha > 1$, the solidification temperature increases with confinement and if $\alpha < 1$, confinement lowers the melting point.

When an IL electrolyte is in the presence of an electrode, interfacial effects arise, owing to steric constraints, electrical-field interactions and chemical or electro- chemical reactions. Studying the electrolyte properties alone is insufficient for developing and evaluating EES devices. The next sections describe the molecular-level structure of the electrode–IL electrolyte interface and the impact of interfacial effects on device performance.

Interfacial ion arrangement

An electrical double layer (EDL) forms when two layers of opposite charge accumulate at an electrode–electrolyte interface separated by an atomic-scale distance, as first described by Helmholtz in the nineteenth century. The electric potential drops across the EDL and its response to charging governs the electrical capacitance at the interface. The structure of an EDL defines and controls the energy that is stored in an EDL capacitor (also known as a non-faradaic supercapacitor). For a redox process, the driving forces are the voltage difference between the electrodes and the positions where

the electrochemical reactions occur. The potential distribution in the EDL determines the electrochemical kinetics of a battery; that is, the electrochemical current follows an exponential relationship with the voltage difference across the interface. This section describes the structure of the electrode–IL interface and the change in the ion arrangement caused by variation of the applied potential (Fig. 3).

Theoretical understanding of the EDL

The Stern-modified Gouy–Chapman model, which consists of a Stern layer with compact adsorbed ions and a diffuse layer with a continuous distribution of the electrolyte's cations and anions, describes a general EDL of a salt-in-solvent electrolyte on a charged surface (Fig. 3a). In a dense, liquid-like IL environment, the structure of the EDL differs considerably from that of a diluted counterpart, owing to the stronger ionic interactions present in neat ILs. In 2007, Kornyshev proposed a model to describe the interfacial capacitance of a metal–IL system by solving the Poisson–Fermi equation, which treats the electrolyte using a mean-field lattice-gas model, and derived an analytical expression for the differential capacitances of local concentrations of different ions[36]. The model predicted that, when the ionic concentration changes from low to high, the differential capacitance curve changes from a 'Bactrian-camel' shape to a 'bell' shape because of the crowding effect at high concentrations; in other words, there is no room to pack more counterions on the electrode surface to compress the double layer, and thus the thickness of the double layer has to increase with the voltage. This effect cannot be captured by the traditional Stern–Gouy–Chapman model. Independently, Bazant and colleagues derived the same analytical solution by solving a modified Poisson–Nernst–Planck equation to describe the ion transport during dynamic charging at a large bias voltage[37]. The transition in the shape of the differential capacitance curve upon increasing the ionic concentration is well reproduced by classical density functional theory (DFT) based on a coarse-grained molecular model of ILs[38]. Classical DFT also predicted alternating cation–anion layered structures of up to ten layers on a strongly charged surface[39].

To further explain the differential capacitance curve, Bazant, Storey and Kornyshev developed a simple Landau–Ginzburg-type continuum theory of the EDL for an electrode–IL system[40]. The model predicts that, at small electrode polarization, a charged surface will be overscreened by a monolayer of counterions (Fig. 3b), and the excess charge will be neutralized by abundant co-ions in the second layer[40]. Bazant, Storey and Kornyshev further addressed the crossover from overscreening to crowding with voltage in their theory, whereas Fedorov and Kornyshev had previously investigated the same crossover using MD simulations[41]. Limmer constructed a theory for strong interionic correlations at a metal–IL interface that predicted a first-order transition that leads to spontaneous charge-density ordering at the interface, driven by the applied potential[42]. For details of the theoretical understanding of the variation in EDL structure with applied potential, we refer readers to reF.[43].

Experimental observation of the EDL

The overscreening of ILs manifests as oscillating layers of ions normal to a charged interface, as first reported by Mezger et al. on a sapphire (0001) surface[44]. Fenter and colleagues conducted integrated X-ray reflectivity and classical MD simulations on [BMIM][TFSI] near charged and uncharged graphene surfaces, showing alternating cation-rich and anion-rich layers extending several layers out from the graphene surface, consistent with earlier work[45]. Neutron reflectometry also provides information on the population of a specific ion on an electrode surface, but direct observation of the ion arrangement of layered EDLs is challenging, owing to the limited wavevector transfer range[46]. However, atomic force microscopy (AFM) is an efficient method for detecting both

the ion arrangement on a surface and the layered structure of the EDL. Amplitude-modulated AFM revealed the ordered lateral packing behaviour of [EMIM][TFSI] on a highly ordered pyrolytic graphite electrode[47] (Fig. 3c). The structure of ion layers beyond the first layer was also probed by AFM force measurements for $[PYR_{14}][FAP]$ (where $[FAP]^-$ is tris(penta-fluoroethyl)trifluorophosphate) and [EMIM][FAP] on a charged Au(111) surface[48]. A layered structure of ions extends for around four to seven layers, with a more stable layered structure under negative polarization (cations adsorbed at the interface) compared with positive polarization (anions adsorbed at the interface). Using electrochemical AFM and classical MD simulations, a similar strong and alternating cation– anion layering of [BMIM][TFSI] was observed on graphite surfaces, extending at least five layers from the surface[49].

The molecular-level arrangement of ILs at a surface under an applied potential can be changed by varying the composition of the ions and the alkyl chain lengths. For example, $[EMIM]^+$ with a short tail (ethyl group) forms a stronger interfacial structure than $[BMIM]^+$ (butyl group), as the imidazolium ring of $[EMIM]^+$ is oriented more parallel to the Au(111) surface. By contrast, the packing of $[HMIM]^+$ (1-hexyl-3-methylimidazolium) is more orderly than that of [BMIM]+, as its longer tail increases solvophobic interactions[50]. In addition, the alternating cation-rich and anion-rich layers formed with pyrrolidinium-based ILs transform into a cationic bilayer structure with interdigitated alkyl chains once the length of the alkyl chain on the cation increases from C_8H_{17} to $C_{10}C_{21}$ (REF.[51]). Notably, the neutral alkyl chains on the cations can increase the capacitance at small and intermediate voltages, because they function as latent voids that can be replaced by charged groups to increase the local concentration of charges[52].

The ordered lateral packing structure of an IL does not fully cover an electrode surface, as was observed using AFM when the scanning area was increased from tens of nanometres to hundreds of nanometres. Adsorbed $[PYR_{14}][TFSI]$ forms an ordered lateral structure with stripe-shaped domains of a few hundreds of nanometres in length on uncharged, highly ordered pyrolytic graphite53. The orientation of the stripes is induced by the hexagonal graphite substrates, as indicated by the 120° angle between domains of different orientation. Although the ions adsorbed outside of the domains do not form an ordered lateral structure, the layered structure of the IL normal to the surface is almost the same as that in the domains. The ordered lateral structure in the domains disappears when a large potential is applied ($V < -0.6$ V or $V > 0.4$ V versus open-circuit potential (OCP)).

Effects of changing potential

The structure of an EDL in an IL changes with the applied potential or, more specifically, as the amount of surface charge at the interface is varied (Fig. 3). A neutral state represents the state at which there is no specific adsorption of cations or anions on the electrode surface, and the potential of this state might not be zero. For example, a Au(100) surface in [BMIM][BF4] has a potential of approximately −0.65 V (versus Pt) in its neutral state[54].

X-ray reflectivity was used to investigate the dynamic response of the layered structure of [MNIM][TFSI] (where [MNIM]+ is 1-methyl-3-nonylimidazolium) on pristine epitaxial graphene surfaces during potential cycling as a function of temperature[55]. The IL exhibits different, well-defined, alternating cation–anion layered structures at positive and negative surface potentials (versus OCP). Both structures are present during cycling through the OCP, forming a hysteretic intermediate mixture with a characteristic lifetime on the order of seconds. The temperature dependence of the restructuring (25–60 °C) indicates an energy barrier of ~0.15 eV between the distinct cation-adsorbed (at the negatively charged surface) and anion-adsorbed (at the positively charged surface) structures. This finding is consistent with AFM observations, which indicate that, even at the OCP, the interfacial IL is organized into alternating cation-rich and anion-rich layers at a

local level near the electrode surface[56]. Results from a neutron reflectometry study of [PYR_{14}][TFSI] on a gold electrode support this observation, revealing an excess of cations at the interface in the uncharged state[46]. Increasing the positive charge of the electrode decreases the concentration of the cations at the interface. By contrast, a slight increase in the negative polarization increases the cation excess, with the cations forming a loosely adsorbed layer, which is the initial stage in the formation of the over screening structure.

The loosely adsorbed layer formed during the initial stage of cation adsorption transforms into an ordered structure with increasing negative polarization and, thus, an increasing population of cations. For example, this behaviour was observed using amplitude-modified AFM for [EMIM][TFSI] on a highly ordered pyrolytic graphite surface as the potential was changed from −0.1 to −0.3 V (versus the uncharged state)[47] (Fig. 3c). Upon further increasing the negative polarization, cations reorient from close to parallel to vertically aligned with a slight incline to the electrode surface[57] (Fig. 3d). For example, for a Au(111) electrode in [PYR_{14}][TFSI], the reorientation of the cations was observed using a video scanning tunnelling microscope when the potential was slightly decreased from −1.4 to −1.6 V (versus Pt) (Fig. 3e). Although it was possible to observe the interfacial structure on a sub-second timescale using a video scanning tunnelling microscope, application of a less negative potential (>−1.0 V versus Pt) leads to featureless images, as the time resolution is insufficient to capture images of ILs with rapid dynamic fluctuation.

Under a certain amount of surface charge (σ) and with ions of a specific diameter and charge, a transition from a highly oriented multilayered structure to a surface-frozen monolayer of highly compact counterions (a Moiré-like structure) may occur[58]. With an increase in the surface charge, the transition starts when a dimensionless surface-charge-compensation para- meter $\kappa = |\sigma/\theta^{max}|$ is >0.5 (where θ^{max} is the maximum charge density that can be stored in a monolayer for a specific IL ion), and becomes a dense monolayer of counterions when $\kappa = 1$ (REF.[59]).

As the potential is further increased, the over screening structure transitions into a ‘crowding’ structure, in which counterion adsorption dominates the first two monolayers from the electrode surface, while the co-ions move to the third layer to balance the excess charge[40] (Fig. 3f). The crowding structure was observed by operando X-ray scattering on a silicon electrode with [THTDP][TFSI] (where $[THTDP]^+$ is trihexyltetra- decylphosphonium) as the electrolyte[60] and by neutron reflectometry on a niobium electrode with [THTDP] [PFPB] (where $[PFPB]^-$ is tetrakis(pentafluorophenyl) borate)[61].

Effect of interfacial reactions on the ESW

An IL-based supercapacitor stores charge by counterion adsorption on the charged electrode and the formation of an EDL (Fig. 1c, left). For a conventional IL-based LIB, the IL functions as a ‘solvent’ to dissolve the Li salt, and only Li ions intercalate and deintercalate at the cathode and anode and contribute to the capacity (Fig. 1c, right). However, for dual-ion LIBs, anion intercalation occurs at the cathode, enabling dual-ion batteries to operate at higher voltages than those of normal LIBs.

Although ILs have good electrochemical stability compared with other electrolytes, IL-based EES devices still have a limited ESW, owing to undesired electrochemical reactions at the electrode (Fig. 4a). Compared with a supercapacitor (in which the ESW is mainly limited by interfacial electrolyte decomposition), more diverse and complex irreversible interfacial reactions occur in a LIB, including the co-intercalation of organic ions, electrolyte decomposition, SEI formation and the formation of ‘dead’ Li. The ESW of a dual-ion LIB is also influenced by the type of anion and the concentration of the electrolyte[62]. Solid-state Li^+ intercalation also affects the ESW of the device, as the process is

accompanied by the irreversible transformation and collapse of the electrode crystal structure; we do not discuss this further, as the process does not occur at the IL–electrode interface, and readers are referred to REF.[63] for details. Undesired electrochemical reactions at the interface can also trigger self-discharge mechanisms, shorten the cycling life and raise safety concerns, owing to the loss of active electrode materials, structural damage, gas release and electrolyte consumption. To increase the energy density of IL-based EES devices and ensure their safe operation, it is crucial to understand the possible interfacial reactions and the effect of temperature on these reactions.

Interfacial electrochemical reactions

Irreversible intercalation of organic cations. To simplify the electrolyte in an IL-based LIB, a Li salt with the same anion as the IL can be used. The Li ions in the electrolyte are likely solvated by anions and form $[Li(anion)_x]^{(x-1)-}$ complexes (such as $[Li(TFSI)_2]^-$ in the case of a binary mixture containing Li[TFSI])[64]. Complexation increases the hydrodynamic radius of Li^+, and the electrolyte viscosity increases with an increase in Li salt concentration, resulting in decreased electrolyte ionic conductivity. Before Li^+ intercalation in an IL-based LIB, decomplexation (or desolvation) of the $[Li(anion)_x]^{(x-1)-}$ complex occurs at the electrode–electrolyte interface and liberates the anions. The interaction between Li^+ and the anions substantially affects the interfacial charge-transfer process during ion intercalation[65]. For example, the charge-transfer resistance at the electrode–electrolyte interface in a LIB comprising a Li-metal anode and $LiCoO_2$ cathode with various Li salts dissolved in an N,N-diethyl-N-methyl-N- (2-methoxyethyl)ammonium-based IL strongly depends on the anion; among various anions, the system with the $[FSI]^-$ anion exhibits the lowest charge-transfer resistance[66] (Fig. 4b).

The presence of organic cations causes competitive intercalation with Li^+. For example, in an electrolyte comprising Li[TFSI] and [EMIM][TFSI], $[EMIM]^+$ inserts into a layered graphite electrode at a potential of ~1 V (versus Li/Li^+) during an initial cathodic scan[67]. The intercalation of the organic cations is usually irreversible and destroys the layered structure of the anode, compromising performance. To prevent the intercalation of organic cations, the intrinsic intercalation properties of the electrode materials and the electrolytes should be considered. Combining $[EMIM]^+$ with the $[FSI]^-$ anion suppresses the intercalation of the organic cations, allowing reversible Li^+ intercalation at 0–0.2 V (versus Li/Li^+) on graphite[67]. One possible explanation for this behaviour is that the decomposition of [FSI]– during the initial charging cycle leads to the formation of a passivating SEI that prohibits the intercalation of $[EMIM]^+$ (REF.[68]). Moreover, intercalation of organic cations is prohibited if the electrode material allows Li^+ to intercalate at a relatively positive potential compared with the decomposition potential of $[EMIM]^+$. For example, a titanium oxide bronze (TiO_2-B) electrode operates stably in a voltage window of 1.2–2.5 V with a Li[TFSI]–[EMIM][TFSI] electrolyte, because the lithiation–delithiation potential (~1.5 V versus Li/Li^+) lies within the ESW of [EMIM] [TFSI] (REF.[69]). Similarly, lithiated titanium oxide, with a redox potential of 1.5 V (versus Li/Li^+), is a suitable anode for a full-cell device with an IL-based electrolyte in combination with a high-potential cathodic material, such as $LiCoO_2$ (REF.[70]).

Electrolyte decomposition at the interface. Linear-scan voltammograms of ILs with the $[TFSI]^-$ anion (Fig. 4c) show that the irreversible cathodic (reductive) decomposition of $[EMIM]^+$ occurs at an electrode potential of 0.9 V (versus Li/Li^+) or −2.6 V (versus Fc/Fc^+)[71], which are more positive potentials than the intercalation potential of Li^+ in a graphite electrode (0.1 V versus Li/Li+) and the potential for Li-metal plating (0 V versus Li/Li^+). Using electrochemical surface enhanced Raman spectroscopy, it was shown that [EMIM][TFSI] on a Ag surface decomposes into an N-heterocyclic carbene, which degrades further through dimerization[72].

Methylimidazole and ethylimidazole can also be generated through dealkylation side reactions. The imidazolium $[BMIM]^+$ has a moderately low reductive stability, owing to the acidic proton at the C2 position[73]. Hence, functionalizing the C2 position of imidazolium cations with an alkyl group, such as in 1,2-dimethyl-3-propylimidazolium[74], enhances the electrochemical stability of imidazolium cations. Compared with imidazoliums, aliphatic quaternary ammoniums, including pyrrolidinium and piperidinium[71,75], and aliphatic quaternary phosphoniums[76] exhibit a higher reductive stability. Moreover, relatively large ions, such as 1-alkyl-3-methylimidazolium ($[CnMIM]^+$) and N-alkyl-N-methylpyrrolidinium ($[CnMPYR^+]$) with $n \geq 4$, $[TFSI]^-$ and $[FAP]^-$, are electrochemically more stable, owing to the presence of stable functional groups and the increased distance from the electrode[59,77]. A DFT study revealed that mixing ILs may also expand the ESW by decreasing the potential of zero charge[78]. As the driving force of electrochemical redox reactions is the potential difference between the reaction position and the electrode surface, the ion arrangement in the EDL may also influence the kinetics of redox reactions under an applied potential.

Dendrite growth during Li plating. Li metal, which exhibits the highest theoretical specific capacity and the lowest electrochemical potential among anode materials, is again attracting substantial interest following significant breakthroughs in suppressing dendrite growth[79–81]. Dendrite growth at the interface between Li metal and a liquid electrolyte can result in short-circuiting and battery fires, decreasing the cycling life and causing safety concerns. The efficiency of Li plating and stripping is promoted at elevated temperature, suppressing the incidence of dendritic deposition[82]. Thus, in theory, Li-metal anodes can operate efficiently at elevated temperatures until they reach their melting point of 180 °C.

Suppression of Li whisker-like dendrite growth has been observed using the IL electrolyte $[PYR_{14}][TFSI]$ and was attributed to rapid formation of an SEI, which prevents direct exposure of the metal surface to the electrolyte and enables the uniform deposition of Li beneath the SEI[83]. The SEI layer on the Li-metal anode forms from rapid decomposition of $[TFSI]^-$ initiated by C–S and/or S–N bond cleavage, whereas the cation is stable[84,85]. The unusual reductive decomposition of $[TFSI]^-$, observed experimentally and theoretically, occurs owing to charge transfer from Li metal to the anion. However, when $[BF4]^-$ is the anion, no charge transfer was observed from the Li metal to the anion, making the cation more prone to decompose[84].

Avoiding a deep-charge state by using electrode materials with high Li intercalation potentials, such as Li-rich titanium oxides, possibly mitigates Li plating and dendrite growth[86]. However, using a Li-rich titanium oxide narrows the operating voltage window and leads to a decreased energy density. A liquid metal alloy, composed of Sn and Ga, shows self-healing properties as a liquid and, when used as an anode, can sufficiently limit dendrite growth and prolong the cycling life[87]. Moreover, anodes with curved surfaces are less susceptible than flat surfaces to the vertical growth of dendrites, because the stronger binding between the anode and Li^+ regulates the interfacial mass and/or charge transfer towards uniform Li plating[88]. Adding an artificial protective layer between Li metal and the electrolyte may also solve the dendrite problem, if the protective layer is flexible enough to accommodate electrode-volume changes during cycling and low electrical conductivity to avoid direct Li deposition on the protective layer [89,90].

SEI layer formation. Irreversible electrochemical reactions at the electrode–electrolyte interface may lead to the formation of an insulating SEI layer, which prevents contact of the organic solvent or organic cations with the electrode materials, thus, increasing the stability of the electrode in the charged state. Moreover, the SEI layer can sieve out reducible organic cations and solvents, allowing reversible Li^+ intercalation and deintercalation outside the ESW of the IL-based electrolyte. Additionally, the formation of an SEI layer, such as that formed by adding ethylene sulfite to

[PYR_{14}][TFSI]–Li[TFSI], can enhance the coulombic efficiency of both Li+ and anion intercalation in a dual-ion battery91. However, an SEI layer does not necessarily prevent undesired reactions. For example, PC can form an SEI layer at 0.9V (versus Li/Li+), but PC still intercalates, together with Li+, into a graphite electrode. The co-intercalation of PC results in exfoliation of graphite and the destruction of the electrode[92].

The ability of different organic solvents and ILs to form an SEI is related to the energy of their highest occupied molecular orbital (HOMO) and lowest unoccupied molecular orbital (LUMO)[93,94]. A low-lying LUMO level increases the reduction potential, making SEI formation more facile, whereas a low-lying HOMO suggests increased stability towards oxidation, indicating that the material is a good choice for overcharge protection. The choice of the electrode material affects the HOMO and LUMO levels of a specific electrolyte. For example, Li(100) can lower the LUMO of $[TFSI]^-$, leading to unusual reductive decomposition of $[TFSI]^-$ and the formation of a film on the anode[84]. Although the redox potentials, in some cases, show a strong correlation with HOMO energies, there are suggestions that the HOMO and LUMO energies of a solvent do not directly indicate which species are participating in the redox reaction[95]. Instead, the Gibbs free-energy difference between the reactants and products, which includes all electrolyte components, correlates directly with the redox potential and the SEI-formation ability.

In an emerging strategy, ILs can be designed to form stable SEI layers on both the anode and the cathode. For example, carbonate-functionalized imidazolium cations combine the advantages of ILs with those of traditional carbonate electrolytes[96]. Similarly, anions can also be functionalized to participate in the formation of stable SEI layers[97]. After addition of lithium bis(2-methyl-2-fluoromalonato)borate to a carbonate electrolyte, a stable and thin SEI layer was observed on a $LiNi_{0.5}Mn_{1.5}O_4$ electrode after only one pre-cycle[97].

Effects of high temperature

Increasing the temperature not only accelerates the kinetics of reactions that occur at room temperature but also initiates chemical or electrochemical side reactions. Cyclic voltammetry was used to investigate the room-temperature and high-temperature electrochemical stability of different ILs (including [EMIM][TFSI] and [PIP][TFSI] (where $[PIP]^+$ is 1-methyl-1-propylpiperidinium)) and a carbonate-based electrolyte with Li[TFSI] on a TiO_2- B electrode[69] (Fig. 4d,e). Comparing the cyclic voltammograms obtained at 25 and 120 °C, the lithiation process evolves into three separate pairs of redox reactions, indicating that the rates of deintercalation and intercalation are increased at higher temperatures. The onset reduction potential of $[EMIM]^+$ is 0.6 and 1 V (versus Li/Li^+) at 25 and 120°C, respectively, suggesting that reduction is promoted at higher temperatures. Although anodic decomposition is suppressed when pyrrolidinium-based and piperidinium-based ILs are used, the decomposition-free voltage still shifts from 0.5 to 1.0 V at the elevated temperature, indicating shrinkage of the ESW. The compatibility of the IL with different electrode surfaces is crucial to the electrochemical stability at elevated temperature. Some cation and anion combinations have lower onset temperatures for thermal runaway than that of conventional EC:DEC electrolytes on specific charged electrode surfaces; for example, the runaway temperatures for [EMIM][FSI] and EC are 70 and 140 °C, respectively, on $Li_7Ti_5O_{12}$ and 225 and 325 °C, respectively, on $Li_{0.45}CoO_2$ (REF.[98]).

Owing to the decreased ESW at elevated temperatures, operating a device within the same voltage window as at room temperature lowers the coulombic efficiency of Li^+ intercalation and deintercalation as a result of the formation of a thick SEI film that blocks Li^+ intercalation and increases the impedance[69,99]. For example, for a graphite electrode in an organic solvent, the thickness of the SEI increases with ascending temperature, resulting in a 50% increase in cell

impedance at 70 °C (REF.[99]). A thin SEI layer formed on a Si anode at 60 °C when using an IL electrolyte free of organic solvent (0.5 M Li[FSI] in [PYR_{13}][FSI], where [PYR_{13}]$^+$ is 1-methyl-1-propyl-pyrrolidinium). Compared with the thick film formed in a carbonate-based electrolyte (1 M Li[PF_6] in fluoroethylene carbonate:DMC), the IL-derived thin film enables longer, more stable device operation at 60 °C (REF.[100]). In another example, [PIP] [TFSI]–Li[TFSI] affords an SEI layer on a Si anode that is thicker than that of an organic electrolyte (1 M Li[PF6] in EC:DEC)101. Adding PC into the [PIP][TFSI]– Li[TFSI] mixture increases the contribution of the [TFSI]– decomposition product to the composition of the SEI and decreases the thickness of the SEI layer. The SEI layers formed by the reduction of the IL-based electrolytes (with or without PC) are stable up to 100 °C, and the LIB operates at 100 °C with the same cycling stability as at room temperature. Moreover, IL-derived films formed on a graphite electrode at 90 °C, using Li[TFSI] in [PYR13][TFSI], [PIP][TFSI] or [BMIM][TFSI], are thicker and more thermally resilient than the corre- sponding films formed at 25 °C (reF.102). Although the thicker films show increased charge-transfer resistance, the capacity of the electrodes covered by the thicker films, surprisingly, increases at a low rate (<0.1 C), likely due to improved wetting of the electrode by the electro- lyte and higher Li+ transference numbers in the films. Additionally, increasing the concentration of a Li salt (Li[FSI]) in trimethylisobutylphosphonium bis(fluoro- sulfonyl)imide enhanced the mechanical stability of the resultant SEI, which remained intact on the Si electrode after 60 cycles at 80 °C (reF.103).

There is no report of an SEI layer that is stable at tem- peratures comparable to those at which SEI-free electro- des stably operate; for example, a LiFePO4 cathode in molten Li[TFSI] operates at 250 °C (reF.104); a Li4Ti5O12 anode in an electrolyte comprising Li[TFSI], [PIP][TFSI] and boron nitride at 150 °C (reF.105); and a carbon electrode in [BMIM][TFSI] at 200 °C (reF.106). Thermal breakdown of the SEI layer, which leads to the build-up of internal resistance and continuous consumption of electrolyte and electrode materials, also limits electrochemical sta- bility at elevated temperatures. For electrodes such as Si that undergo large volume expansion and/or shrinkage during the charge and discharge processes, decomposi- tion of the SEI is more profound at elevated temperatures when the rate of Li+ intercalation and deintercalation is faster107. To construct an SEI that is thermally stable at high temperature, the electrolyte, Li salt and electrode must be considered. Ongoing research should focus on understanding the mechanism of SEI formation and its dependence on anode–electrolyte–cathode combi- nations to develop a strategy to design SEI layers with improved thermal stability and cycling performance.

Increasing the electrochemical stability

Ionic interactions and reversible interfacial reactions can be exploited to enlarge the ESW. The ionic interactions between Li^+, anions and additives (protic IL, solvents and glymes) must be fine-tuned to facilitate Li^+ decomplexation at the electrode–electrolyte interface and to maximize the electrochemical stability of electrolyte. Meanwhile, the addition of redox-active electrolytes can introduce reversible interfacial reactions at the cathode, impeding the irreversible oxidation of the electrolyte.

Protic ILs are intrinsically limited as electrolytes for LIBs because the acidic proton is reactive towards Li metal[108,109]. However, deprotonation does not occur when the water content is <20 ppm (REF.[110]). Thus, using the protic IL [Et3NH][TFSI] (where [Et3NH]$^+$ is triethyl- ammonium) with 1 M Li[TFSI], a $LiFePO_4$//$Li_4Ti_5O_{12}$ LIB demonstrates stable operation111. Unlike in aprotic ILs, the strong interaction between protic cations and anions means that both Li^+ and protic cations are coordinated by the anions in the electrolyte. This competition for the anions decreases the coordination number of Li^+ with anions; in other words, the Li ions are shielded by fewer anions in a protic IL. Thus, it is easier for Li^+ to dissociate from its anions at the electrode–electrolyte interface, decreasing the

charge-transfer resistance and improving the rate performance. On a lithium vanadium phosphate electrode, the protic IL [$PYRH_4$] [TFSI] (where $[PYRH_4]^+$ is N-butylpyrrolidinium) with Li[TFSI] exhibits Li^+ intercalation with an obvious lithiation platform at a potential of ~0.6 V (versus Ag). In comparison, Li^+ intercalation is less facile with the aprotic analogue, Li[TFSI]–[PYR_{14}][TFSI], which shows a much smaller Li^+ intercalation platform at a higher potential of ~0.7 V (versus Ag). Moreover, the lithiation potential in this protic IL is even lower than that of 1 M Li[PF_6] in EC:DMC (~0.65 V versus Ag)[112].

Compared with neat ILs, solvent-in-IL electrolytes show increased ionic conductivity without narrowing of the ESW[113,114]. Adding a small amount (20% (v/v)) of a carbonate to a piperidinium-based IL did not lower the thermal stability compared with the solvent-free IL, but the ionic conductivity increased, owing to weakened Li^+–anion interactions in the large $[Li(anion)x]^{(x-1)-}$ clusters[101]. For a protic IL, the coordination number of Li^+ with $[TFSI]^-$ (~1) is much lower than for an aprotic IL (~2)[115]. Addition of 20 wt% PC to a protic IL and an aprotic IL results in a 20% and 50% reduction in Li^+– $[TFSI]^-$ coordination, respectively[116], demonstrating that Li^+ decomplexation is easier in the aprotic IL. The solvent-in-salt approach has also been applied to develop non-flammable LIB electrolytes. A solvent-in-salt electrolyte using a flame-retardant solvent, trimethyl phosphate, was applied on carbon anodes. The LIB exhibited increased thermal stability and a fire-extinguishing capability with similar device performance to that of a LIB using a conventional flammable carbonate electrolyte[117]. When added to a Li salt, glyme chelates Li^+, yielding $[Li(glyme)]^+$ complexes that are stable and long-lived; hence, [Li(glyme)][TFSI] can be considered an IL[118]. The chelated salts [Li(triglyme)][TFSI] and [Li(tetraglyme)] [FSI] have a melting point of 23 °C with a super-cooled state over a wide temperature range, and are used as electrolytes in batteries. Chelated triglyme–Li salts become more resistant to oxidation as the ratio of Li^+ to triglyme decreases from 20 to 1, owing to the strong interaction between Li^+ and triglyme[119]. Diluting the IL with a solvent increases the ionic conductivity of the electrolyte but at the risk of lowering the resistance to oxidation. However, diluting chelated glyme–Li salts with hydrofluoroether increases the ionic conductivity without lowering the oxidation resistance, as the structure of $[Li(glyme)]^+$ is undisturbed by the addition of hydrofluo- roether, owing to the stronger attraction between Li^+ and glyme than that between Li+ and hydrofluoroether[120].

To ensure battery safety at enlarged ESWs, redox-active pairs can be added as additive redox shuttles to avoid overcharging at the cathode. In an over-charged state, these redox-active additives are oxidized at the cathode–electrolyte interface, serving as an over-charge shunt to decrease overcharge damage to the electrode and electrolyte[26]. The oxidized redox-active additives diffuse to the anode and are reversibly reduced to their initial state. Ideally, a redox shuttle has an oxidation potential higher than the maximum potential of the charged cathode and lower than the electrolyte decomposition potential. For more information about redox-active electrolytes, readers are referred to REF.[121].

IL-based solid-state electrolytes

Replacing flammable and volatile organic solvents with solid-polymer electrolytes in a solid-state battery significantly improves the safety[122]. Addition of an IL into the solid-polymer electrolyte, such as [PYR_{14}][TFSI] into Li[TFSI]–poly(ethylene oxide), decreases the interfacial resistance between Li metal and the polymer electrolyte, suppressing Li dendrite formation[123]. The low ionic conductivity of polymer electrolytes (~10^{-5}–10^{-6} S cm^{-1}) limits their application in practical devices. Decreasing the Li^+–anion association energy by using a delocalized anion is one approach to increase the ionic conductivity. By dissolving a Li salt with a highly delocalized poly- anion in a poly(ethylene oxide) host, a high ionic conductivity (1.35×10^{-4} S cm^{-1}) was achieved at 90 °C (REF.[124]). Polymeric ILs,

which function as polymer hosts for Li salts, form free-standing films with high mechanical and electrochemical stability, and are used as polymer electrolytes for LIBs. A pyrrolidinium-based polymeric IL with Li[TFSI] and containing 50 mol% of plastic crystal succinonitrile exhibits a high room-temperature ionic conductivity of 5.74×10^{-4} S cm^{-1}, which is 600 times that of the sample without succinonitrile[125]. A free-standing gel polymer electrolyte composed of a pyrrolidinium-based polymeric IL and Li[TFSI] achieves a room-temperature ionic conductivity of up to 3.35×10^{-3} S cm^{-1} when 80 wt% of [EMIM][TFSI] is added[126].

Combining ILs with responsive polymers opens new avenues for electrolytes to prevent thermal runaway. The use of a Li salt dissolved in an IL–polymer mixture is reported for some LIB cells. Such combinations are reliable for operation at temperatures between 90 and 120 °C, as they are thermally and electrochemically stable, pro- viding a high ionic conductivity[127,128]. To mitigate thermal runaway and extend battery lifetime, safety mechanisms have been developed to shut off operation at high temperatures. For example, an IL-doped polymer electrolyte that undergoes a phase transition at high temperature, resulting in a reversible increase in internal resistivity, has been used to render a LIB inoperable at temperatures above 140 °C. Thermally activated phase separation between the polymer, poly(benzyl methacrylate), and IL, [EMIM][TFSI], occurs at ~105 °C. Increasing the concentration of Li^+ from 0 to 1 M elevates the lower-critical solution temperature of the polymer from 100 to 140 °C, owing to a 'salting in' phenomenon, which prevents the polymer from phase separating and, hence, maintains the viscosity and conductivity of the electrolyte[127]. The reversibility of the polymer response remains an issue upon cooling in such systems. Additives, such as allylboronic acid pinacol ester and N-heterocyclic carbene adducts, can form a passivating film on the cathode at a specific potential to shut down the overcharge[129,130]. However, polymerization of these shutdown additives is typically irreversible. To make the shutdown process reversible, a thermoresponsive polymer switching material was developed comprising graphene-coated spiky Ni nanoparticles in a polymer matrix. Upon overheating, expansion of the polymer matrix separates the conductive nanoparticles and shuts down the conductive pathways; when the temperature is lowered, the material shrinks and regains its conductivity[131].

Polymer-based separators tend to soften or shrink upon heating, limiting their long-term stability beyond 100 °C. The compatibility of several conventional separators with IL electrolytes has been examined[132]. Two examples of separators that operate at high temperature with an IL electrolyte are Li superionic conductor, which operated at 80 °C (REF.[133]), and a composite bentonite clay, which has operated in LIBs at temperatures of up to 120 °C and in supercapacitors at up to 200 °C (REFs[106,134,135]). Unfortunately, the bentonite clay contains additional ions that hinder Li^+ diffusion and create a concentration overpotential. Hexagonal boron nitride, a layered material with no additional ions, is a promising alternative to bentonite clay for high-temperature operation; successful application of a full-cell LIB with a $Li_4Ti_5O_{12}$ anode and a $Li_{1+x}Mn_{2-x}O_4$ cathode at 120 °C was reported using a mixture of boron nitride powder and Li[TFSI]–[PIP][TFSI] as the electrolyte[105].

Charge-storage capability

The structure of the EDL determines the number of ions that are electrochemically adsorbed on the flat surface of an electrode and, thus, the charge-storage capability of ILs per unit of surface area. In the above, we discussed the structure of EDLs on flat metallic and graphenic surfaces without confinement. However, porous carbon, the most widely used supercapacitor electrode, is neither ideally metallic nor flat. The electric field of the ions penetrates through the pore walls, leading to a slight weakening of the screening from ionic interactions between the ions and the wall, increasing the distance between the adsorbed ions and the carbon electrode, compared with the distance to a metal electrode. The complexity of the porous structure and the steric limitations of the pore size

also create a confined environment that breaks the layered structure.

Compared with metallic surfaces, graphenic electrode materials can induce additional interactions with specific ions, such as π–π interactions with imidazolium rings. The heterogeneous features of graphenic electrodes, including reactive edge sites[136], defects[56] and surface functional groups[137,138], also influence the ion arrangement at the IL–electrode interface. The impact of the surface chemistry on the ion arrangement and the capacitance must be considered together with the effects of confinement. For example, surface hydroxyl groups attract anions closer to the pore walls, even at a negatively charged surface (with a surface-charge density of −4.0 μC cm^{-2})[137] and restrain the anion orientation and mobility (such as for trifluoromethanesulfonate[139] and [TFSI]− (REF.[140])). On a nonporous graphene surface without confinement, the hydroxyl groups lower the capacitance of the negative electrode, as the counterion (cation) accumulation density is lower[137]. However, the negatively charged slit-shaped pore of carbide-derived carbon (CDC; with a surface-charge density of −5.0 μC cm^{-2}) can accommodate more cations, because the anion arrangement increases the likelihood of the cations accumulating in the pore centre and adjusting their orientation from parallel (0° to the surface) to vertical (90° to the surface). Enlarging the ion-accessible surface area through the incorporation of nanopores was considered a promising strategy to increase capacitance. In 2006, an anomalous normalized capacitance (capacitance per surface area) enhancement was observed in pores smaller than 1 nm (REF.[141]), demonstrating that the pore size is an important parameter that influences capacitance[142]. Both classical MD and classical DFT simulations reveal that surface-area-normalized capacitance displays an oscillatory dependence on pore size, owing to the overlap- ping EDLs and excluded-volume effects related to the finite diameters of the ions[143–145]. Partial desolvation in sub-nanometre pores explains the decrease in surface area occupied per ion, confirmed by classical DFT simulations[146], and leads to an increase in capacitance in solvent-containing electrolytes. For a neat IL, the dramatic increase in the normalized capacitance is explained by a mathematical model that assumes close packing of the ions in pores[147]. Pore volume directly correlates to the normalized capacitance, and pore-volume utilization is maximized when the pore size matches the ion size. To design a realistic supercapacitor electrode material to approach the theoretical capacitance limit in a specific IL, the pore-size distribution should be narrow, ideally monodispersed, with an average size selected carefully based on the ion size and operating voltage[148]. Moreover, as quantitatively revealed by a Monte Carlo simulation, the interpore connectivity can significantly influence the effective pore-size distribution and, hence, the capacitance[149].

The effect of temperature on the EDL also influences the charge-storage capability of IL-based EES devices. Disruption of the interfacial EDL structure at higher temperatures, as observed by in situ scanning tunnelling microscopy and in situ AFM, lowers the capacitance[150]. Moreover, as elevated temperature weakens the ion–electrode interactions, the distance between the electrode surface and the adsorbed ions increases, which may decrease the capacitance[44]. The Debye length, a characteristic length that describes how the surface charge is screened by the electrolyte, is also temperature-dependent and influences the EDL[40].

Transport-limited charge storage

Impact of ion transport

The above factors determine the theoretical charge-storage capability, regardless of transport limitations. However, ion-diffusion resistance leads to a rapid drop-off in the charge-storage capability, especially at high scan rates and low temperatures. Ion diffusion in long pores leads to large ohmic drops, causing a lag in the build-up of electrode charge with applied potential, even at a very low scan rate[151]. Enhancing the conductivity of the electrode is one approach to decrease the

ohmic drop, as a highly conductive material shows close to ideal capacitive behaviour with a lower diffusion resistivity[152]. Otherwise, using highly conductive materials as a conductive backbone for electrochemically active materials with low conductivity can also enhance the high-rate performance.

In addition to the ohmic loss, the ionic conductivity drops in nanoscale pores, as ion transport is hindered by friction from the charged electrode surface and ion– ion interactions. An X-ray study of the crowding ion structure reveals an ultra-slow ion-diffusion mechanism at the interface between methyltrioctylammonium bis(trifluoromethanesulfonyl)imide and a conductive Si electrode, indicating that in-pore ion diffusion may also involve long-length-scale rearrangements[153]. Hence, the average diffusion coefficient of the ions in the electrode is one or two orders of magnitude lower than that in the bulk and neat IL electrolyte[154].

Long and tortuous diffusion pathways, as well as curved, defective and functionalized pore walls, influence in-pore ion diffusion. However, there are indications that an ultra-long ion-diffusion length does not necessarily lead to a large capacitance loss[155] and/or that ion transport within a confined environment can be faster than in the less confined electrolyte between particles of the electrode material[156]. Using electrochemical impedance spectroscopy, an increase in ion-diffusion length was observed in a CDC material upon increasing the electrode thickness from 90 μm to 1 mm.

Nevertheless, despite the 11 times increase in electrode thickness, the drop in specific capacitance was only 18%. Moreover, a CDC electrode with a particle size of 75 μm showed comparable impedance to a CDC electrode with a 5-μm particle size in both neat [EMIM][TFSI] and solvated [EMIM][TFSI]. The origin of the influence of active-material particle size and electrode thickness on specific capacitance requires further study[157].

Charging mechanism

Using pulsed-field gradient NMR, ion diffusivity was observed to decrease linearly with an increase in in-pore ion population (Fig. 5a), demonstrating the dominant impact of in-pore ion population on in-pore diffusion[158]. The movement of cations and anions in opposite directions, bypassing each other, is key to increasing the ion-diffusion resistivity in confined pores. The impact of the charging mechanism on the in-pore ion population is discussed in the following sections.

Impact of charging mechanism on ion diffusion. Once a potential is applied to an electrode, the IL ions start to diffuse in the pores with a lag of few seconds, as observed by Fourier transform infrared spectroscopy on a CDC electrode in [EMIM][TFSI][159]. Assuming ions already occupy pores at zero potential, three possible processes can occur at the interface between the bulk electrolyte and the in-pore electrolyte: counterion adsorption (X = 1), counterion and co-ion exchange (X = 0) and co-ion desorption (X = −1), where X is the charging mechanism parameter and is defined based on the impact of the mechanism on the in-pore population (Fig. 5b).

The value of X can vary from −1 to 1, indicating combined charging mechanisms[160]. The charging mechanism of the pores is affected by the polarization of the electrode and the type of electrolyte. On the basis of the correlation between the ion population and the applied potential, the charging mechanism of YP-50 activated carbon in 1.5 M $[PEt_4][BF_4]$–ACN is dominated by ion exchange with positive polarization and is closer to counterion adsorption with negative polarization[161]. For a pure IL, the charging mechanism tends to show combined features with a non-integer X value, owing to stronger ionic associations. For example, the charging process on YP-50 activated carbon with $[PYR_{13}][TFSI]$ combines ion exchange and counterion adsorption (X = 0.3) when positively charged and is in between ion exchange and co-ion desorption (X = −0.4) when negatively charged[162].

Moreover, the state of charge influences the charging mechanism. Using electrochemical quartz crystal microbalance (EQCM), it was shown that the charging mechanism changes from ion exchange to anion absorption as the positive voltage of a CDC electrode increases in [EMIM][TFSI][163].

The charging mechanism affects in-pore ion diffusion by influencing the in-pore ion population. For a neat IL, MD simulations suggest that the volume occupied by the electrolyte ions shows almost no change between a charged and a discharged state when the charging mechanism is dominated by ion exchange[164]. Otherwise, there is a change in the in-pore ion population that corresponds to the charging process. Counterion adsorption increases the in-pore ion population, and the resistance grows as more ions are adsorbed. Conversely, desorption of co-ions decreases the ion population and is beneficial to in-pore ion diffusion.

Impact of ion wettability on the charging mechanism. For ionophilic materials, electrolyte ions diffuse into the pores of an uncharged electrode; hence, porous electrode structures are filled with electrolyte ions even before charging, as was confirmed using in situ NMR[151]. The NMR signal shifts once the electrolyte is in contact with the electrode, corresponding to the access of ions to the carbon electrode. Moreover, NMR spectroscopy offers quantitative information regarding the ion species inside the pores, and thus the populations of cations and anions can be differentiated. For example, the cation and anion populations inside porous YP-50 activated carbon simultaneously and equally increase with an increase in concentration of $[PEt_4][BF_4]$ (where $[PEt_4]+$ is tetraethylphosphonium) in bulk ACN[161].

NMR does not provide information about the porous structure[165], but such information is acquired using other techniques, such as neutron scattering[166]. In situ small- angle neutron scattering reveals pore-size-dependent ion-adsorption properties, as the contrast between the carbon electrode and the void space vanishes once pores with specific sizes are occupied. With ACN, incomplete wetting behaviour is observed inside the smallest pores (~0.4 nm) of activated carbon[167]. However, solvent-free [BMIM][TFSI] uniformly distributes on the electrode surface under zero potential, even in the smallest micropores with pore sizes of ~0.75 nm (reF.168). Moreover, the in-pore ion population in YP-50 activated carbon in $[PYR_{13}][TFSI]$ ismmol g−1, which is much larger than the ion popula- tion of 0.9 mmol g−1 in 1.5 M $[PEt_4][BF_4]$ in ACN, indicating a positive correlation between the ion concentrations in the bulk electrolyte and inside the pores[160].

The charging mechanisms described above are all based on ionophilic materials with pores that are initially filled (Fig. 5b). MD simulations predict that, if pores are ionophobic, initially unfilled pores would aid in-pore ion diffusion[169]. In this scenario, a single-file charging mechanism is proposed[170] and ion diffusion in ionophobic pores with a slit pore shape is predicted to be faster than in the bulk electrolyte at a moderate voltage[171]. To decrease the in-pore ion population, especially for ILs with stronger ionic interactions, requires electrolyte– electrode coupling to facilitate counterion desorption or an ion-exchange mechanism, but has yet to be realized, and an ionophobic electrode also remains to be developed.

The mechanism of charging, especially in narrow pores, is an interesting topic for theory and simulations. Using an improved mean-field model, it was predicted that ionophobic pores (initially empty) charge faster in a waveform propagation, whereas charging of ionophilic pores (initially filled with ions) occurs diffusively[172]. Furthermore, it was shown that the ionophobicity of nanopores can be used to maximize energy storage[169]. Coarse-grained MD simulations revealed that overfilling or de-filling slows down charging of ionophilic sub-nanometre pores[171]. By contrast, all-atom MD simulations indicated faster-than-bulk ion diffusion at moderately high surface-charge densities in ionophilic pores. The difference in these findings was attributed to the difference in ion shape

between the coarse-grained model (roughly spherical) and the all-atom simulations, and to the decrease in total ion density and looser ion packing at higher surface-charge densities[154].

Impact of confinement on the charging mechanism. Pore size influences the charging mechanism and capacitance at an applied potential. When the applied polarization increases, larger pores (pore width/ion diameter = 1.2) show two stages of charging: adsorption of counterions at low potentials and expulsion of co-ions or ion exchange at higher potentials[173]. In the case of smaller pores (pore width/ion diameter = 1–1.08), the capacitance vanishes instantly when the potential reaches a critical value and no second step is allowed because of the stronger steric interactions resulting from the highly confined geometry. Monte Carlo simulations, by contrast, have suggested that abrupt counterion adsorption occurs at a critical potential and that very few counter-ions enter the pores before that potential is reached. The potential-induced adsorption of counterions becomes less abrupt (and may fade) with increasing pore size[174]. Experimental evidence is required to further understand this field-induced change in mechanism and the influence of pore size. As the capacitance depends on both the pore size and the applied potential, an optimized pore size and surface energy will afford the highest energy density in a wide potential window[148]. For more accurate prediction of the maximum energy density of a specific electrode material, both the capacitance– voltage relationship and the pore-size distribution must be considered[175].

Atomistic MD simulations provide further insight into ion transport during the charging process. Classical MD simulations revealed pore-size-dependent charging behaviour: when the pore size is comparable to the ion diameter, ion diffusivity exceeds the bulk values; however, for wider pores, ion diffusivity is below bulk values[154]. Simulations of charge cycling of ILs in sub-nanometre slit pores finds distinct ion-transport properties at different locations inside the pores: fast ion migration near the entrance but slow dynamics inside the pore[176]. Classical MD simulations also suggest that, in a fast-charging cycle, electroneutral co-ion and counterion pairs may be trapped inside the pores, leading to decreased capacitance[177].

Charge storage at low temperature

When the average rate of in-pore ion diffusion is lower than the charging rate, the ion accessibility of pores is limited with a higher resistance, lowering the capacitance. This problem is exaggerated at low temperatures by the decrease in ionic conductivity and, hence, the in-pore ion-diffusion coefficient of a supercapacitor. At low temperatures, the energy-storage process in a supercapacitor will eventually become diffusion-controlled, with a substantial decrease in the specific capacitance. According to a 1D Ising model of single-file metallic nanopores, a higher potential is required to break the strong, ionic cation–anion association at low temperatures[178]. Moreover, at low temperatures, a higher potential is required as the driving force for ions to access narrow and terminal pores, further lowering the capacitance.

At the electrode–electrolyte interface of a LIB, decomplexation of Li^+–anion complexes is more difficult at low temperature, because the ion-dissociation energy is also temperature-dependent. The impedance of the SEI layer should also be higher for ion transport at lower temperatures[179]. For the same applied voltage (same driving force), the higher ion-diffusion resistance at low temperature obstructs the access of ions to the active sites in the matrix of a material, in turn, lowering the capacity of the battery. The formation of Li dendrites also becomes more severe at a deep-discharge state and low temperature, owing to the slower plating of Li at the electrolyte–electrode interface. For a dual-ion battery, in which more than one ion participates in the charge-storage process, the diffusivity difference as well as the temperature effect on each type of ion must be taken into consideration. The slow diffusion of one specific ion leads to an ion concentration gradient from the

positive electrode to the negative electrode, influencing the viscosity and the ionic conductivity of the electrolyte and, thus, the charging process[180]. Although the solid-state intercalation of Li is not the focus of this Review, it is worth mentioning that a drop in temperature will also impede the capacity of a battery by kinetically obstructing charge transfer between Li^+ and the electrode surface. For example, the charge-transfer resistance of a $LiFePO_4$ cathode increases by >300% when the operating temperature decreases from room temperature to −20 °C (REF.[181]).

Low ion-diffusion-resistance electrodes

To assist ion diffusion, especially at low temperatures, the electrode materials should feature ion-transport channels with low resistivity. In situ diffusion NMR spectroscopy reveals that a slight increase in the average pore size substantially increases the average diffusion coefficient[158]. Macropores with a low level of confinement allowed the storage of electrolyte in its bulk form, enabling a reduction in the ion-transport length from the bulk electrolyte reservoirs to the mesopores and micropores[182]. However, introducing macropores into the materials reduced the volumetric capacitance of the electrodes. By contrast, introducing mesopores as well as nitrogen doping in a porous carbon promoted rate capability when the ion dynamics in the micropores were the rate-limiting factor[183]. Quasielastic neutron scattering integrated with classical MD simulations shows that an oxidized CDC surface exhibits stronger surface adsorption of the electrolyte ions compared with the non-oxidized CDC surface, which is beneficial for potential-driven ion transport during charging[137].

An open structure, which is affected by the material morphology and dimensions, is also crucial for ensuring an efficient ion-diffusion pathway. For example, onion-like carbon, or nonporous carbon, exhibits close to ideal capacitive behaviour with lower diffusion resistivity in [EMIM][TFSI] compared with a CDC material, as the ions move very small distances, adsorbing onto the carbon onion surface during charging[159]. Compared with a stacked carbon onion, vertically aligned carbon nanotubes provide an efficient ion-diffusion pathway with low resistance, and almost no capacitance loss is observed when the temperature decreases from room temperature to −50 °C in a mixed IL electrolyte[4]. However, the absolute value of the capacitance is low, as the surface areas and packing densities of both the carbon onions and the aligned carbon nanotubes are moderate.

Two-dimensional layered materials enable high packing densities and spontaneous ion intercalation from all their side facets. Large ions, including IL ions and solvated ions, can be accommodated between the layers, as the interlayer spaces of a 2D material are flexible. Introducing spacers in between 2D layers, such as carbon nanotubes[184,185], polymers[186], metal-oxide nanoparticles[187] or large ions[188], increases the interlayer spacing, enlarges the accessible surface area and increases ion transport rates. Moreover, a vertically aligned 2D titanium carbide MXene electrode, produced using a liquid-crystal method, shows thickness-independent capacitance, indicating substantial ion accessibility within the 2D material[189].

A 3D templated framework provides a large specific surface area and efficient access for electrolyte penetration, although the pore size must be well designed to avoid excessive reduction of the volumetric capacity. With a 3D interconnected structure, an activated graphene electrode can deliver a high specific capacitance of 100 F g^{-1} at temperatures as low as −40 °C, in a 1:1 mixture of [PIP][FSI] and $[PYR_{14}][FSI]$[190]. The cell still operates at −50 °C; however, the estimated equivalent series resistance, based on impedance spectroscopy, shows a 100-fold increase when the temperature decreases from room temperature to −40 °C, and the cell becomes diffusion-controlled, with a severe capacitance drop at low temperatures. Hence, focusing only on the material aspect to decrease the ion-transport distance and offer an open structure is still insufficient to extend the low

temperature window.

Ionic interactions to assist ion diffusion

Superionic state. When ILs with a strong ionic association between the cations and anions are used, both types of ions enter the pores simultaneously during the charging process. For example, regardless of the potential polarization (1.5 and −1.5 V), infrared spectroelectrochemistry measurements confirm that both $[EMIM]^+$ and $[TFSI]^-$ enter the pores of a CDC electrode[159]. The simultaneous access of co-ions and counterions to the porous structure decreases the capacitance by neutralizing the charges; it also increases the in-pore ion population and reduces ion diffusivity.

Co-entering of co-ions and counterions is mitigated in highly confined pores when a 'superionic state' is activated[191]. A superionic state partially breaks the coulombic ordering, owing to the screening of electrostatic interactions by free electrons on the electrode pore wall[173]. Therefore, for [EMIM][TFSI], the coordination between anions and cations weakens in 0.7-nm pores compared with that in the bulk electrolyte and 1-nm pores. Moreover, the close packing of like-charged ions in a highly confined structure enhances the normalized capacitance. After being predicted by a phenomenological model[173] and confirmed by Monte Carlo simulations[192], the superionic effect was observed experimentally through X-ray scattering measurements combined with a Monte Carlo simulation to recover the structure of the IL in carbon nanopores. A frequent anion–anion pairing is observed in 0.7-nm pores (Fig. 5c), whereas almost no anion pairing is observed for 1-nm pores[191]. The reduced distance between the like-charged ions in the pores can possibly increase the ion packing density on the electrode surface and the theoretical capacitance.

MD simulations also demonstrate that the ion-diffusion coefficient in nanoconfined pores is insensitive to temperature variations, unlike in bulk electrolytes. Although the simulations were not performed for IL systems, they may, nonetheless, indicate a possibility for reduced cation–anion interactions in confined nanostructures[193]. As ionic associations may also be reduced in a superionic state between oppositely charged ions, smaller pore sizes would not necessarily lead to a smaller ion-diffusion coefficient.

Solvation and desolvation. Adding solvent facilitates ion diffusion in pores by reducing the ionic association between cations and anions, and preventing direct contact of the ions with the pore walls, where their dynamics are severely hindered[194,195]. The charging mechanism can change from an intermediate mechanism (X is non-integer) for a neat IL to ion exchange or counterion adsorption (integer X values) for a solvent- diluted IL, in which simultaneous adsorption of co-ions is prohibited[161]. The room-temperature capacitance of a supercapacitor is retained at temperatures as low as −100 °C if the pore size is large enough to accommodate the fully solvated ions[196], demonstrating the importance of the in-pore solvation level to ion transport.

The cation solvation number of an electrolyte inside and outside pores can be estimated by combining NMR with EQCM measurements. For example, the cation solvation number in a bulk electrolyte (2 M [EMIM][TFSI] in ACN) was measured to be 8 but decreased to 3–4 in 1-nm pores of a CDC[163]. The desolvated ions exhibit reduced mobility in ångström-scale slit pores[197]. The solvation number in pores decreases as the degree of con- finement increases[198], as observed for [EMIM][TFSI] in ACN using EQCM measurements[163]. The combination of in situ small-angle X-ray scattering measurements and Monte Carlo simulations revealed that the solvation status depends on the carbon nanopore structure and the global ion concentrations in the electrodes, and that the tight interaction between an ion and its solvation shell prevents complete desolvation in carbon materials with sub-nanometre pores[199].

In a solvated IL, the access of solvent molecules to the pores inversely correlates with the ion concentration in the bulk electrolyte. As determined from time-resolved infrared spectra, the access of a PC solvent to a CDC material is barely observable when the PC and [EMIM] [TFSI] have a mass ratio of 9:1. However, the organic solvent can clearly access the pores when using an IL-concentrated electrolyte (mass ratio of 1:1). This effect arises owing to stronger IL–PC solvation in the IL-concentrated electrolyte[159].

Selective ion adsorption. Selective access of specific ions to confined structures may assist in-pore ion diffusion by preventing the pore space being occupied by ions with a large resistance. The accessibility of pores is determined by the relative geometric sizes of the ions and pores, especially for confined pores that are small enough to enable the overlap of EDLs with the channel walls[200]. Ions of different sizes are sieved using pores with various levels of confinement[156], as confirmed by X-ray diffraction[201].

When there is competitive adsorption of two different counterions at the entrance of micropores, ionic interactions also affect ion accessibility. For example, based on solid-state NMR observations, $[EMIM]^+$ selectively accesses negatively charged micropores in the presence of tetramethylammonium ($[Me4N]^+$), even though $[EMIM]^+$ and $[Me4N]^+$ have similar sizes. This selective access results from the stronger ionic association between the anion, $[BF4]^-$, and $[Me4N]^+$ than between $[Me4N]^+$ and $[EMIM]^+$ (REF.[202]) (Fig. 5d). However, $[EMIM]^+$ and $[Me4N]^+$ can simultaneously access mesopores. Interestingly, the simultaneous adsorption of two different cations increased the ion-packing density, owing to cation–π interactions between $[Me4N]^+$ and the ring of $[EMIM]^+$.

Outlook

Efficient EES operation with ILs

The intrinsic properties of IL electrolytes significantly improve the safety of EES devices, even at high temperature. However, to capitalize on the favorable IL properties, the ESW, the charge-storage capability and the rate capability must be maximized to improve the energy and power density of IL-based EES devices (Fig. 6a).

The thermodynamics of the interfacial reactions and overpotential of ILs on various electrode surfaces must be considered to mitigate irreversible interfacial reactions. When irreversible electrolyte–electrode electrochemical reactions are thermodynamically favoured, preventing direct electrolyte–electrode contact (such as through the formation of a thermally and electro- chemically stable SEI layer and precise control of the ionic interactions) is an efficient approach to extend the ESW. To enlarge the charge-storage capability at high rates or low temperature, the ion-transport resistance must be minimized. As ion-transport strongly correlates with the in-pore ion populations, manipulating the charge-storage mechanism is a promising way to increase the charge-storage capability. The ion–electrode and ion–ion interactions can be finely controlled to further assist ion transport.

Beyond current electrode–IL systems

Emerging ILs. New ILs are being developed to improve the charge-storage capability by introducing redox reactions and influencing the interfacial ion arrangement. Functionalized ILs are attracting increasing attention[203], especially bi-redox ILs, which provide an additional redox reaction to enhance the charge-storage capacity of an EES device[204]. Oligomeric ILs can also increase the capacitance, as rearrangement of the IL occurs with a smaller entropy loss than that of monomeric

ILs under an applied electrochemical potential[205]. Another emerging class of IL is surface-active ILs. Surface-active ILs possess an amphiphilic structure, whereby van der Waals interactions between the alkyl chains of the IL lead to electrolyte self-assembly and enhanced charge-storage capability[206].

To minimize resistance-induced capacity loss and maximize the power in an EES device, the ionic conductivity of bulk ILs needs to be further increased. Cation–anion pairs with reduced ionic interactions should offer higher ionic conductivity. Eutectic mixtures of ILs exhibit the lowest melting points and viscosity, thus providing a path to improved performance com- pared with that of single-composition IL electrolytes. Water-in-salt electrolytes also show promising performance in water-based LIBs[207]. The addition of a small amount of water or solvent does not decrease the electrochemical and thermal stability of the IL, while the ionic conductivity increases. IL gel electrolytes (or ionogels) combine the advantages of a non-leaking gel and a non-volatile, thermally stable and safe IL. These electrolytes are therefore promising choices for on-chip and wearable textile devices. Improvements in the ionic conductivity of IL gel electrolytes are needed, and this will require the design of new polymers, self-polymerization of ILs and proper polymer–IL pairing.

Redox-active electrode surfaces with ILs. Materials that enable reversible redox reactions with multielectron transfer remarkably increase the charge-storage capability of LIBs. Transition metal halides, chalcogens and chalcogenides are new multi-electron cathode materials with high theoretical capacities and large operational potential windows. The multi-electron-transfer capability of these materials arises from the breaking and reformation of chemical bonds and multiple phase transformations during the charge–discharge process. Such multi-electron-transfer systems can further benefit from the enhanced electrochemical stability and safety of ILs, without the limitation of the moderate IL diffusivity, as the IL functions only as a solvent for Li^+ transport and the large IL ions are not involved in the bulk transport and intercalation.

Introducing redox reactions is an efficient way to enhance the charge-storage capability and increase the energy density of a supercapacitor. Electrode materials that realize energy storage through fast intercalation reactions and highly reversible surface redox reactions are classified as pseudocapacitive materials, with examples including transition metal dichalcogenides[208], oxides and hydroxides, carbides and nitrides (MXenes)[209]. These materials are attracting significant attention because they have energy densities higher than those of EDL capacitors and rates higher than those of batteries. Again, considerable opportunities exist for combining IL electrolytes with pseudocapacitive materials to provide wider ESWs and to enable redox processes that require a higher potential. The ionogel formed by pre-introducing an IL into the interlayers of a MXene shows a dramatically enhanced volumetric capacitance[210.] Despite the high capacitance already achieved in pseudocapacitive materials with ILs, only limited intercalation reactions have been observed. Hence, there is scope to improve the intercalation and promote the reversible surface redox reactions using ILs, as well as opportunities in applying redox ILs in layered pseudocapacitive materials.

New electrolyte–electrode interfaces. The introduction of new electrode materials and electrolytes leads to new electrochemical and chemical reactions and processes at electrode–electrolyte interfaces (Fig. 6a). Notably, for intercalation within 2D architectures, new interfaces are not limited to the interlayer spaces of a homogeneous material. Compared with 2D sheets of the same kind, packing different 2D materials layer by layer offers a dense heterostructure with distinct electrochemical properties, owing to the asymmetry of the interactions between the two different material layers and the intercalated electrolyte ions. The charge-storage mechanisms and ion transport within these heterogeneous environments remain mostly unexplored, representing an exciting avenue of future research[211].

Recent work demonstrates the importance of considering all aspects of electrode and electrolyte combinations for enhancing the performance of new electrochemical-material systems. The solvent, which does not directly contribute to the capacitance, strongly affects the charge-storage capability in a 2D Ti_3C_2Tx MXene[212] — a phenomenon that has not been observed in traditional carbon materials. Despite the ionic conductivity of Li[TFSI] in PC being lower than that in ACN, the cyclic voltammogram of Ti_3C_2Tx in Li[TFSI]–PC shows strong intercalation reactions, with a capacitance almost twice that in other electrolytes. This example highlights how an electrolyte affects the performance of pseudocapacitors by controlling the ion arrangement and desolvation level between the layers (Fig. 6b,c). Moreover, this example demonstrates that conductivity, viscosity and other properties of the bulk electrolyte are not necessarily good predictors of electrochemical behaviour in confinement and in real electrochemical devices.

There are tremendous opportunities to develop computational simulations, especially machine learning and artificial intelligence approaches, to determine the most promising electrode and electrolyte combinations from innumerable combinations of electrode materials, sur- face functional groups, SEI compositions and electrolytes. New electrode–electrolyte interfaces also call for further development of in situ analyses for the observation of electron-transfer and charge-transfer processes, as well as fast and correlated ion transport with real-space information. In summary, considerable basic science and commercial opportunities for EES devices will emerge from the development of new electrode and electrolyte compositions. Understanding the chemical reactions and interfacial interactions that govern device performance will be the key to future success.

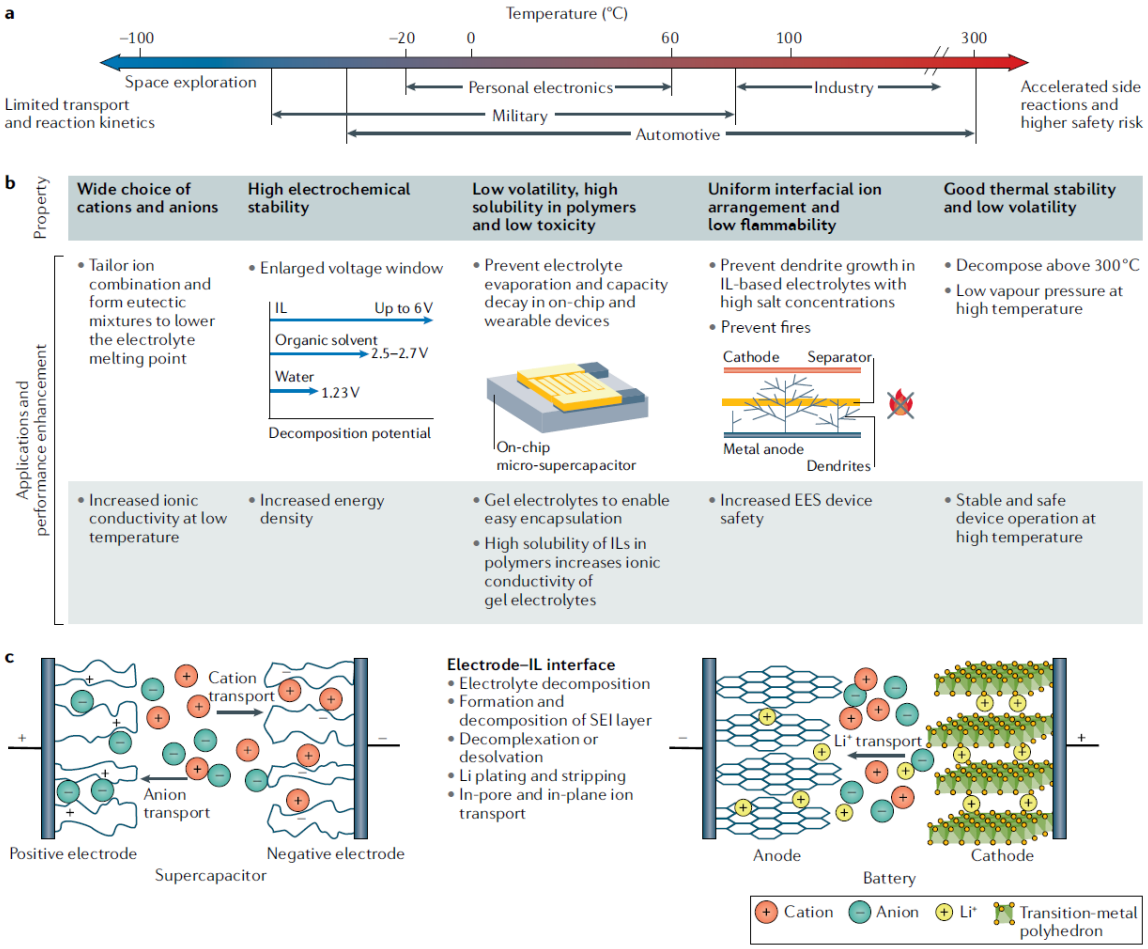

Fig. 1 | **Ionic-liquid electrolytes for electrochemical energy-storage devices. a** | Temperature windows for various applications of electrochemical energy-storage (EES) devices. **b** | Advantages of using ionic liquids (ILs) as electrolytes in EES devices. **c** | Schematics showing the electrochemical processes that occur at the electrode–IL electrolyte interfaces within a supercapacitor and Li-ion battery. SEI, solid electrolyte interphase.

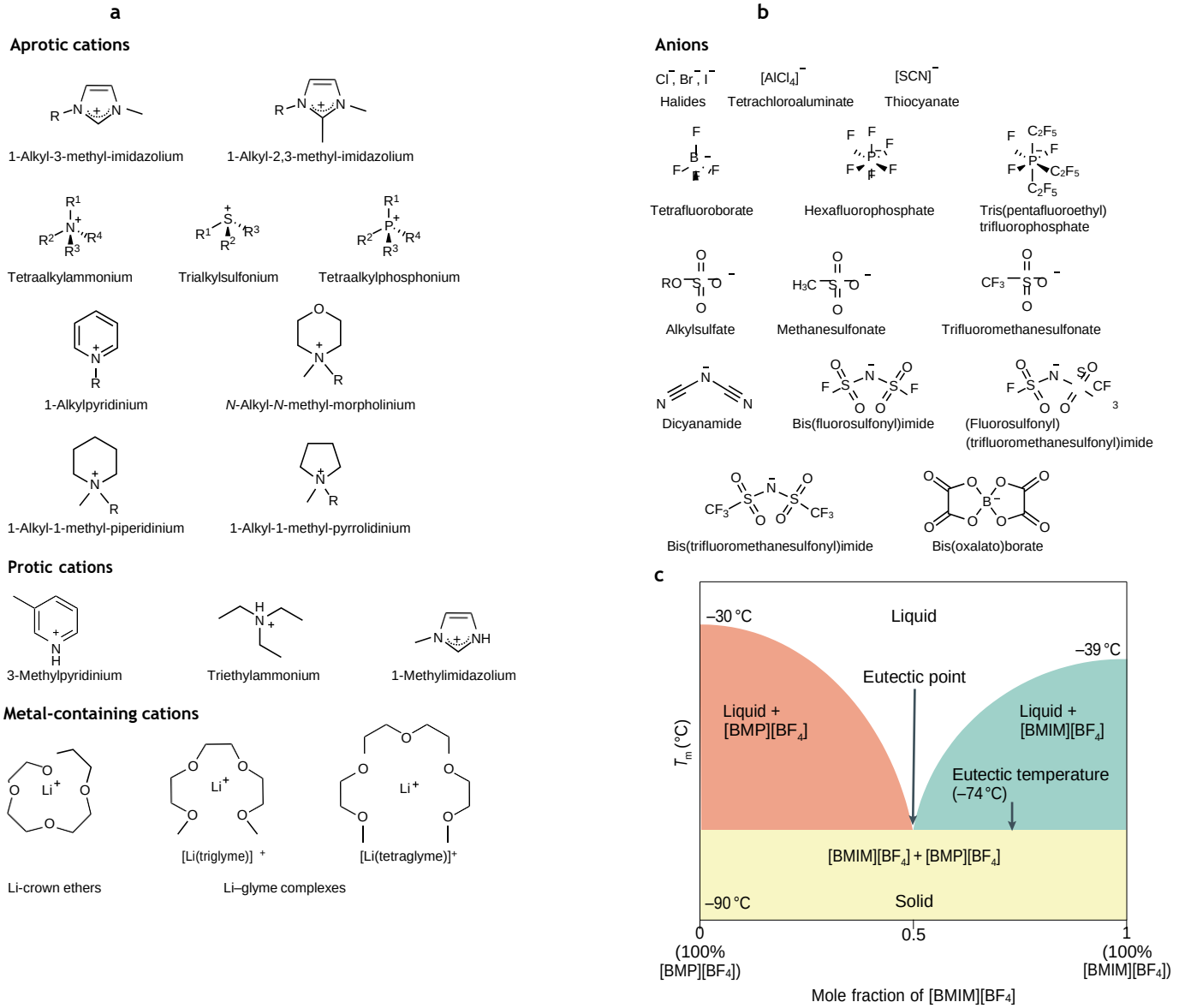

Fig. 2 | **Ionic-liquid ions and properties of ionic-liquid mixtures. a**,**b** | Cations and anions commonly used for the formulation of ionic-liquid electrolytes for energy-storage devices (where R represents an alkyl group, which can be replaced by other groups, such as an olefin, halogen, carbonate, quinone or piperidinyl-1-oxyl). **c** | Proposed phase diagram of a eutectic mixture of 1-butyl-4-methylpyridinium tetrafluoroborate ([BMP][BF_4]) with 1-butyl-3-methylimidazolium tetrafluoroborate ([BMIM][BF_4]). The melting temperatures of [BMP][BF_4], [BMIM][BF_4] and their eutectic phase are −30, −39 and −74 °C, respectively. T_m, melting point.

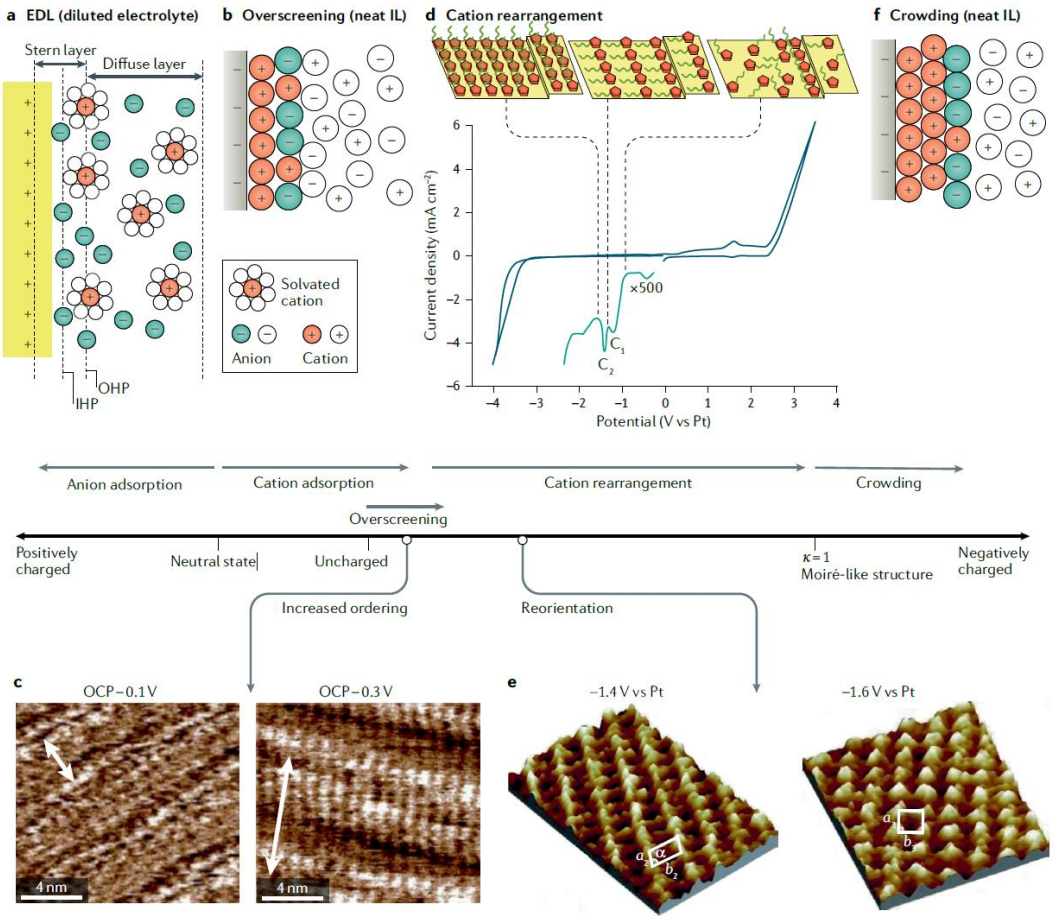

Fig. 3 | **Structure of the ionic liquid–electrode interface.** An electrical double layer (EDL) forms at an electrode electrolyte interface. For neat ionic liquids (ILs), the structuring of ions at the interface is dependent on the applied potential and changes with increasing negative polarization **a** | For an electrode surface in a diluted electrolyte, the EDL comprises a Stern layer and a diffuse layer (where IHP and OHP are the inner and outer Helmholtz planes, respectively). **b** | For a neat IL, the surface charge is overscreened by a monolayer of counterions, and the co-ions in the second monolayer balance the excess charge. **c** | Amplitude-modulated atomic force microscopy images of 1-ethyl-3-methylimidazolium bis(trifluorometh- anesulfonyl)imide ([EMIM][TFSI]) adsorbed on a highly oriented pyrolytic graphite substrate at −0.1 and −0.3 V versus the open-circuit potential (OCP)[47]. The arrows indicate the repeat spacing in the image; as the potential decreases, the adsorbed layer becomes more ordered. **d** | Cyclic voltammogram of a Au(111) electrode in 1-butyl-1-methyl pyrrolidiniumbis(trifluoromethanesulfonyl)imide ($[PYR_{14}][TFSI]$)[57]. Starting from the OCP, two cathodic peaks (C_1 and C_2) are observed in the negative direction and correspond to rearrangement of the cations (as shown in the insets). **e** | The cation rearrangement described in panel **d** was observed in high-resolution scanning tunnelling microscopy images of the $[PYR_{14}]^+$ adlayer on Au(111) at −1.4 V (5.4 nm × 7.5 nm) and −1.6 V (4 nm × 414 nm)[57]. Here, $a_2 = 0.51 \pm 0.05$ nm, $b_2 = 1.01 \pm 0.05$ nm, $a_3 = 0.50 \pm 0.05$ nm and $b_3 = 0.55 \pm 0.05$ nm. **f** | Crowding structure for a neat IL. Counterion adsorption dominates the first two monolayers from the electrode surface, and the co-ions move to the third layer to balance the excess charge. κ, dimensionless surface- charge-compensation parameter. Panels **b** and **f** adapted with permission from REF.[40], APS. Panel **c** adapted with permission from https://pubs.acs.org/ doi/10.1021/acsnano.5b02921 REF.[47], further permissions related to the material excerpted should be directed to the ACS. Panels **d** and **e** adapted with permission from re CH.

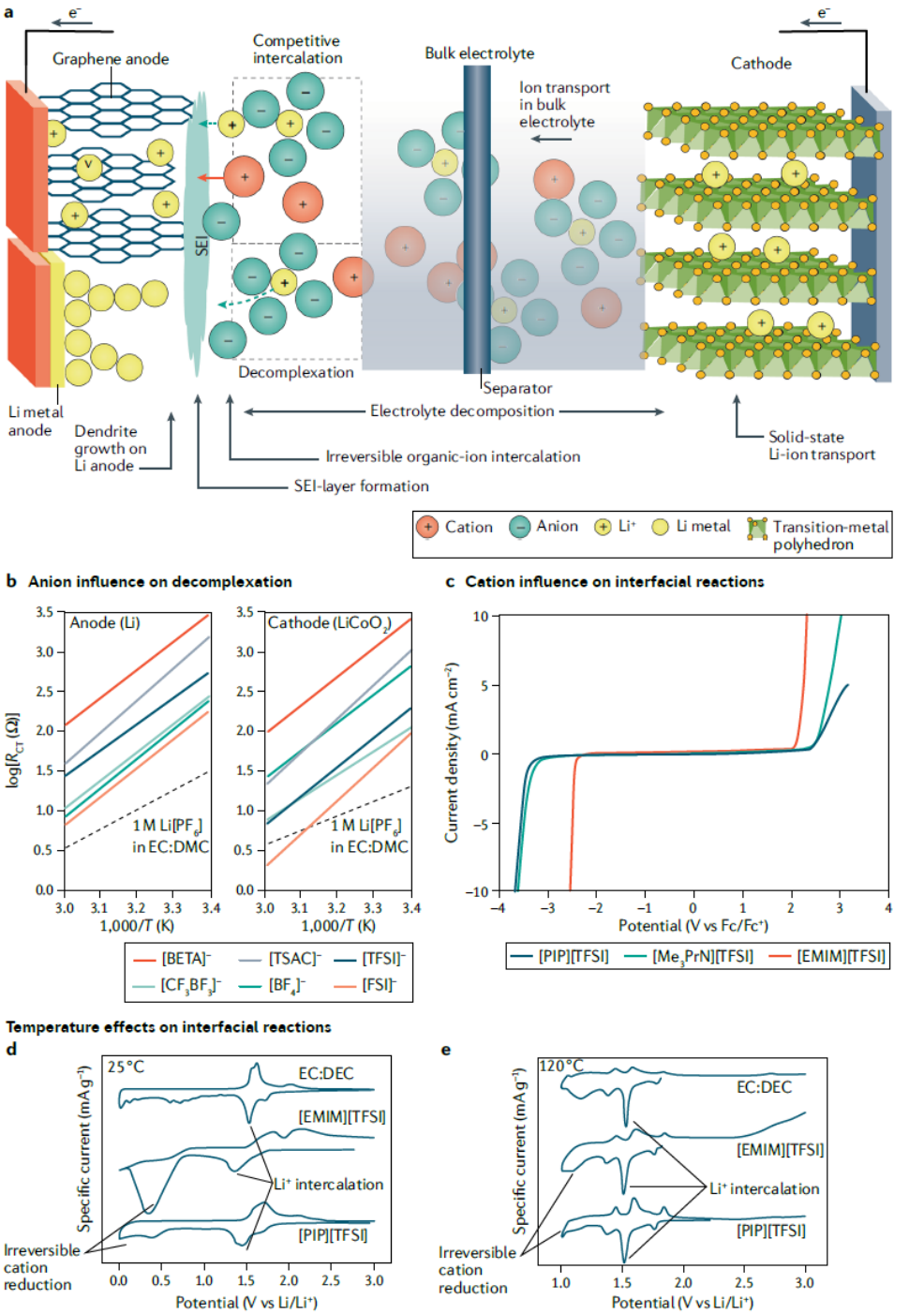

Fig. 4 | **Interfacial reactions. a** | Schematic showing the possible undesirable electrochemical reactions that occur at electrode–ionic liquid (IL) interfaces. **b** | Arrhenius plot of the apparent charge-transfer resistance (R_{CT}) of a $LiCoO_2$ cathode and Li anode in ILs with the *N*,*N*-diethyl-*N*-methyl *N*-(2-methoxyethyl)ammonium cation and various anions (where $[BETA]^-$ is bis(perfluoroethylsulfonyl)imide, $[TSAC]^-$ is 2,2,2-trifluoro-*N*-(trifluoromethanesulfonyl)acetamide, $[TFSI]^-$ is bis(trifluoromethanesul- fonyl)imide and $[FSI]^-$ is bis(fluorosulfonyl)imide). For comparison, the R_{CT} of 1 M lithium hexafluorophosphate ($Li[PF_6]$) in ethylene (EC):dimethyl carbonate (DMC) is also shown. The cell voltage is kept at 4.2 V (REF.[66]). **c** | Linear-sweep voltammograms of $[TFSI]^-$-based ILs with different cations ($[EMIM]^+$ is 1-ethyl-3-methylimidazolium, $[Me_3PrN]^+$ is trimethyl- propylammonium and $[PIP]^+$ is 1-methyl-1-propylpiperidinium) measured at a scan rate of 50 mV s^{-1} at 25 °C. The working and counter electrodes are glassy carbon and Pt, respectively[71]. **d**,**e** | Cyclic voltammograms for a titanium oxide bronze electrode in three different electrolytes (where DEC is diethyl carbonate) with a scan rate of 0.1 mV s^{-1} at 25 °C (panel **d**) and 120 °C (panel **e**) (REF.[69]). SEI, solid electrolyte interphase. Panel **b** adapted with permission from https://doi.org/10.1149/1.3123128, REF.[66], The Electrochemical Society. Panel **c** adapted with permission from REF.[71], Elsevier. Panels **d** and **e** adapted with permission from REF.[69], Elsevier.

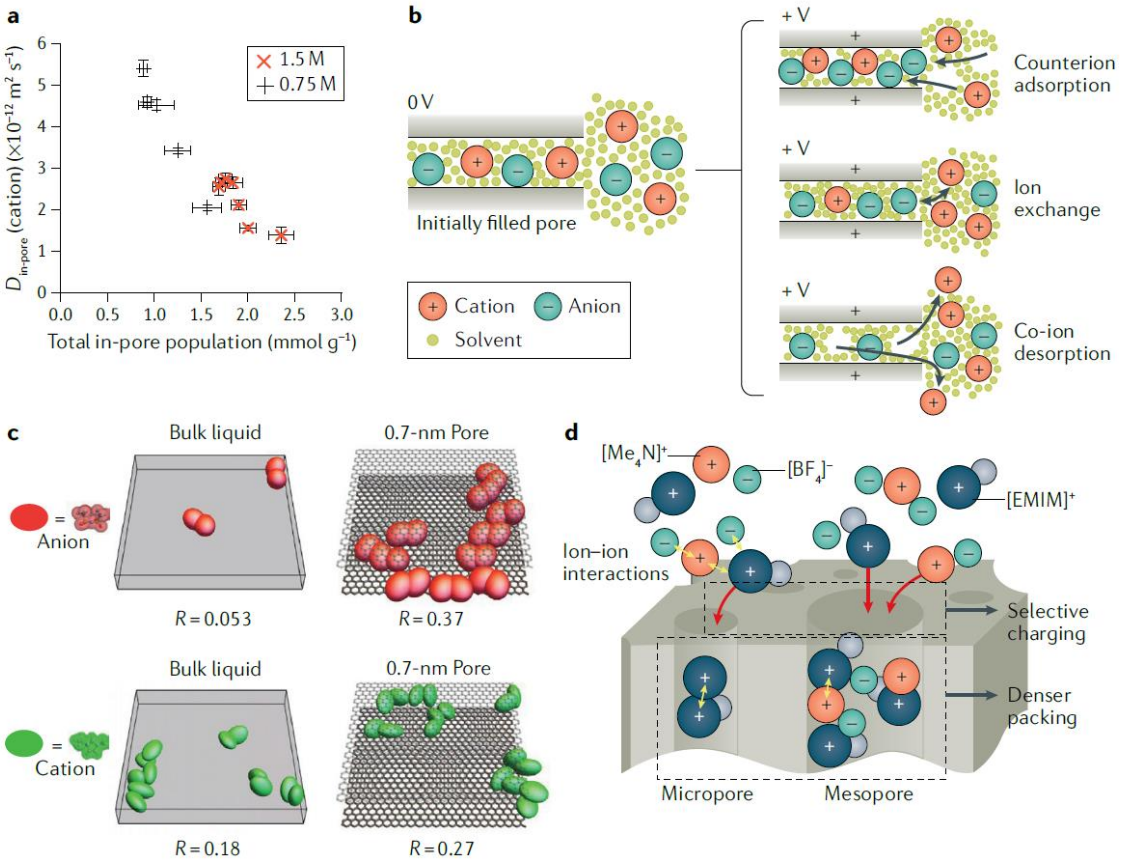

Fig. 5 | **Ion transport and charge-storage capability. a** | Plot showing the inverse correlation between in-pore cation diffusivity ($D_{in\text{-}pore}$) and the total in-pore ion population for an activated carbon electrode in electrolytes with different concentrations of tetraethylphosphonium tetrafluoroborate in acetonitrile[158]. The error bars represent 95% confidence bounds. **b** | For ionophilic pores, which are filled in the uncharged state, there are three charging mechanisms, which result in different changes in the in-pore population of the counterions and co-ions during the charging process[160]. **c** | The superionic state leads to partial breaking of the coulombic ordering in sub-nanometre pores[191]. In bulk 1-ethyl-3-methylimidazolium bis(trifluoromethanesulfonyl)imide ([EMIM][TFSI]), there are few pairs of like-charged ions, whereas numerous pairs are observed in the 0.7-nm pore. *R* is the ratio of the number of paired ions to the total number of ions. **d** | Selective charging of specific ions by controlling the ionic interactions[202]. Yellow arrows represent ionic interactions and the red arrows represent ion diffusion. As the attraction between $[BF_4]^-$ and $[Me_4N]^+$ (tetramethylammonium) is stronger than that with $[EMIM]^+$, only the latter can access the negatively charged micropore. By contrast, both cations can access the less-confined mesopores. Panel **a** adapted from ref.[158], Springer Nature Limited. Panel **b** adapted with permission from ref.[213], RSC. Panel **c** adapted from ref.[191], Springer Nature Limited. Panel **d** adapted with permission from https://pubs.acs.org/doi/10.1021/jacs.7b10693 ref.[202], further permissions related to the material excerpted should be directed to the ACS.

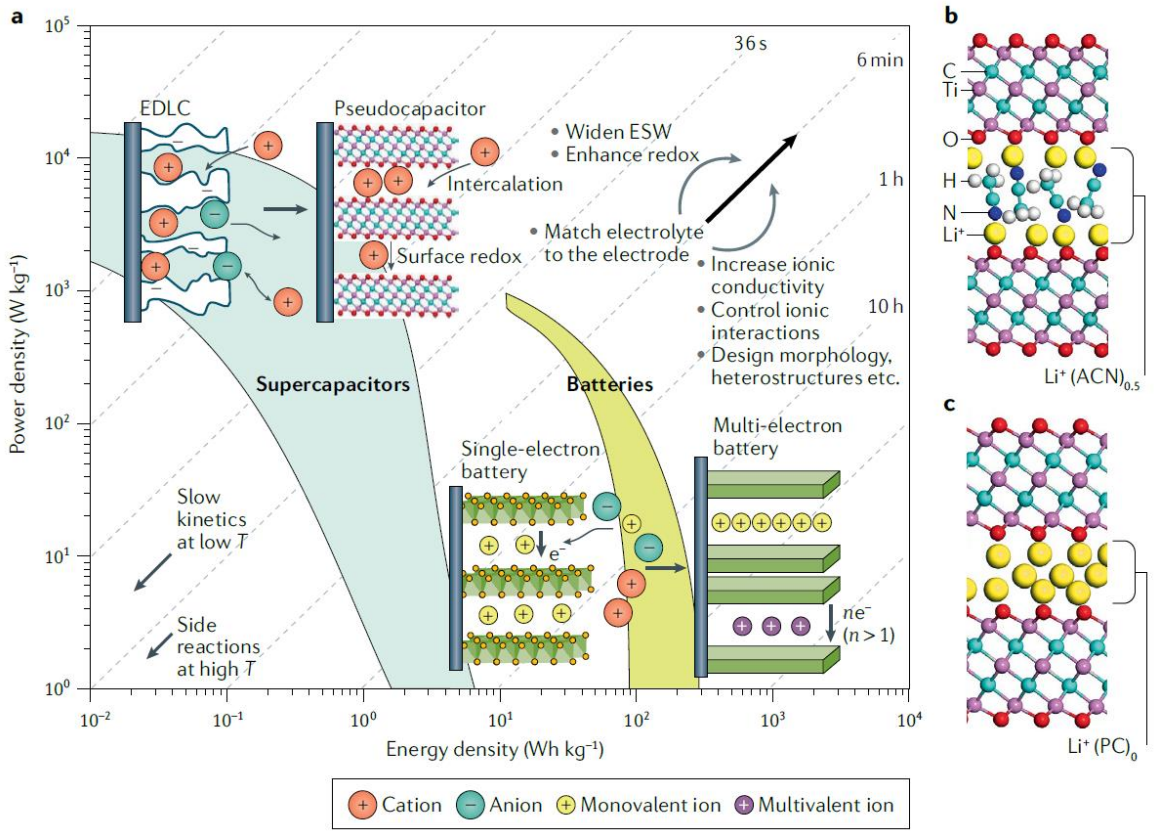

Fig. 6 | **New electrolyte–electrode interfaces. a** | A Ragone plot for electric double-layer capacitors (EDLCs) and Li-ion batteries, summarizing the key strategies to improve the energy and power density. The schematic shows that the introduction of pseudocapacitance (involving pseudocapacitive intercalation and surface redox process) and multi-electron redox processes (involving multi-phase transformations and multi-electron transfers per ion) can increase the energy density of EDLCs and batteries, respectively. The grey dashed lines indicate the time for complete charging or discharging of the device. **b** | A molecular dynamics (MD)-simulated image of a $Ti_3C_2T_x$ electrode in 1M Li[TFSI] (where $[TFSI]^-$ is bis(trifluoromethanesulfonyl)imide) in acetonitrile (ACN), showing the arrangement of ACN and Li ions confined between the charged $Ti_3C_2T_x$ layers[212]. **c** | A MD-simulated image of a $Ti_3C_2T_x$ electrode in 1M Li[TFSI] in propylene carbonate (PC), showing that the Li ions confined between the charged $Ti_3C_2T_x$ layers are fully desolvated[212]. The size of the Li ions is increased for clarity in the simulated images. ESW, electrochemical stability window; *T*, temperature. Panels **b** and **c** adapted from ref.[212], Springer Nature Limited.

References

1. Simon, P., Gogotsi, Y. & Dunn, B. Where do batteries end and supercapacitors begin? *Science* **343**, 1210–1211 (2014).
2. Gogotsi, Y. & Penner, R. M. Energy storage in nanomaterials–capacitive, pseudocapacitive, or battery-like? *ACS Nano* **12**, 2081–2083 (2018).
3. Lin, X., Salari, M., Arava, L. M. R., Ajayan, P. M. & Grinstaff, M. W. High temperature electrical energy storage: advances, challenges, and frontiers. *Chem. Soc. Rev.* **45**, 5848–5887 (2016).
4. Lin, R. et al. Capacitive energy storage from −50 to 100 °C using an ionic liquid electrolyte. *J. Phys. Chem. Lett.* **2**, 2396–2401 (2011).
5. Rogers, R. D. & Seddon, K. R. Ionic liquids–solvents of the future? *Science* **302**, 792–793 (2003).
6. Lian, C., Liu, H., Li, C. & Wu, J. Hunting ionic liquids with large electrochemical potential windows. *AIChE J.* **65**, 804–810 (2019).
7. Armand, M., Endres, F., MacFarlane, D., Ohno, H. & Scrosati, B. Ionic-liquid materials for the electrochemical challenges of the future. *Nat. Mater.* **8**, 621–629 (2009).
8. Jost, K., Dion, G. & Gogotsi, Y. Textile energy storage in perspective. *J. Mater. Chem. A* **2**, 10776–10787 (2014).
9. Sun, X. G., Wang, X., Mayes, R. T. & Dai, S. Lithium–sulfur batteries based on nitrogen-doped carbon and an ionic-liquid electrolyte. *ChemSusChem* **5**, 2079–2085 (2012).
10. Yamagata, M. et al. The first lithium-ion battery with ionic liquid electrolyte demonstrated in extreme environment of space. *Electrochemistry* **83**, 918–924 (2015).
11. Ma, Z., Yu, J. H. & Dai, S. Preparation of inorganic materials using ionic liquids. *Adv. Mater.* **22**, 261–285 (2010).
12. Huang, J. F., Luo, H. M. & Dai, S. A new strategy for synthesis of novel classes of room-temperature ionic liquids based on complexation reaction of cations. *J. Electrochem. Soc.* **153**, J9–J13 (2006).
13. Luo, H. & Dai, S. A new strategy toward synthesis of room temperature ionic liquids based on complexation reactions of cations. *Proc. Electrochem. Soc.* **2004**, 340–345 (2004).
14. Tamura, T. et al. Physicochemical properties of glyme–Li salt complexes as a new family of room-temperature ionic liquids. *Chem. Lett.* **39**, 753–755 (2010).
15. Maton, C., De Vos, N. & Stevens, C. V. Ionic liquid thermal stabilities: decomposition mechanisms and analysis tools. *Chem. Soc. Rev.* **42**, 5963–5977 (2013).
16. Varela, J. C. et al. Piperidinium ionic liquids as electrolyte solvents for sustained high temperature supercapacitor operation. *Chem. Commun.* **54**, 5590–5593 (2018).
17. Lin, X. et al. Thermally-responsive, nonflammable phosphonium ionic liquid electrolytes for lithium metal batteries: operating at 100 degrees celsius. *Chem. Sci.* **6**, 6601–6606 (2015).
18. Watanabe, M. et al. Application of ionic liquids to energy storage and conversion materials and devices. *Chem. Rev.* **117**, 7190–7239 (2017).
19. Yonekura, R. & Grinstaff, M. W. The effects of counterion composition on the rheological and conductive properties of mono- and diphosphonium ionic liquids. *Phys. Chem. Chem. Phys.* **16**, 20608–20617 (2014).
20. Okoturo, O. & VanderNoot, T. Temperature dependence of viscosity for room temperature ionic liquids. *J. Electroanal. Chem.* **568**, 167–181 (2004).
21. Feng, G. et al. Free and bound states of ions in ionic liquids, conductivity, and underscreening paradox. *Phys. Rev. X* **9**, 021024 (2019).
22. Matsumoto, R., Thompson, M. W. & Cummings, P. T. Ion pairing controls physical properties of ionic liquid-solvent mixtures. *J. Phys. Chem. B* **123**, 9944–9955 (2019).
23. Ruiz, V., Huynh, T., Sivakkumar, S. R. & Pandolfo, A. G. Ionic liquid-solvent mixtures as supercapacitor electrolytes for extreme temperature operation. *RSC Adv.* **2**, 5591–5598 (2012).
24. Salari, M., Cooper, B. G., Zhang, H. & Grinstaff, M. W. Synthesis of an environmentally friendly alkyl carbonate electrolyte based on glycerol for lithium-ion supercapacitor operation at 100 °C. *Adv. Sustain. Syst.* **1**, 1700067 (2017).
25. Thompson, M. W., Matsumoto, R., Sacci, R. L., Sanders, N. C. & Cummings, P. T. Scalable screening of soft matter: a case study of mixtures of ionic liquids and organic solvents. *J. Phys. Chem. B* **123**, 1340–1347 (2019).
26. Kalhoff, J., Eshetu, G. G., Bresser, D. & Passerini, S. Safer electrolytes for lithium-ion batteries: state of the art and perspectives. *ChemSusChem* **8**, 2154–2175 (2015).
27. Every, H., Bishop, A. G., Forsyth, M. & MacFarlane, D. R. Ion diffusion in molten salt mixtures. *Electrochim. Acta* **45**, 1279–1284 (2000).
28. Montanino, M. et al. Physical and electrochemical properties of binary ionic liquid mixtures: $(1-x)$ $PYR_{14}TFSI$–(x) $PYR_{14}IM_{14}$. *Electrochim. Acta* **60**, 163–169 (2012).
29. Brennecke, J. F. & Maginn, E. J. Ionic liquids: innovative fluids for chemical processing. *AIChE J.* **47**, 2384–2389 (2001).
30. Taige, M., Hilbert, D. & Schubert, T. J. S. Mixtures of ionic liquids as possible electrolytes for lithium ion batteries. *Z. Phys. Chem.* **226**, 129–139 (2012).
31. Lian, C. et al. Enhancing the capacitive performance of electric double-layer capacitors with ionic liquid mixtures. *ACS Energy Lett.* **1**, 21–26 (2016).
32. Zhou, Y. et al. High performance supercapacitor under extremely low environmental temperature. *RSC Adv.* **5**, 71699–71703 (2015).
33. Chen, S., Wu, G., Sha, M. & Huang, S. Transition of ionic liquid [Bmim][PF_6] from liquid to high-melting-point crystal when confined in multiwalled carbon nanotubes. *J. Am. Chem. Soc.* **129**, 2416–2417 (2007).
34. Kanakubo, M., Hiejima, Y., Minami, K., Aizawa, T. & Nanjo, H. Melting point depression of ionic liquids confined in nanospaces. *Chem. Commun.* **17**, 1828–1830 (2006).
35. Radhakrishnan, R., Gubbins, K. E. & Sliwinska-Bartkowiak, M. Global phase diagrams for freezing in porous media. *J. Chem. Phys.* **116**, 1147–1155 (2002).
36. Kornyshev, A. A. Double-layer in ionic liquids: paradigm change? *J. Phys. Chem. B* **111**, 5545–5557 (2007).
37. Kilic, M. S., Bazant, M. Z. & Ajdari, A. Steric effects in the dynamics of electrolytes at large applied voltages. I. Double-layer charging. *Phys. Rev. E* **75**, 021502 (2007).
38. Jiang, D.-e., Meng, D. & Wu, J. Density functional theory for differential capacitance of planar electric double layers in ionic liquids. *Chem. Phys. Lett.* **504**, 153–158 (2011).
39. Wu, J., Jiang, T., Jiang, D.-E., Jin, Z. & Henderson, D. A classical density functional theory for interfacial layering of ionic liquids. *Soft Matter* **7**, 11222–11231 (2011).
40. Bazant, M. Z., Storey, B. D. & Kornyshev, A. A. Double layer in ionic liquids: overscreening versus crowding. *Phys. Rev. Lett.* **106**, 046102 (2011).
41. Fedorov, M. V. & Kornyshev, A. A. Towards understanding the structure and capacitance of electrical double layer in ionic liquids. *Electrochim. Acta* **53**, 6835–6840 (2008).
42. Limmer, D. T. Interfacial ordering and accompanying divergent capacitance at ionic liquid-metal interfaces. *Phys. Rev. Lett.* **115**, 256102 (2015).
43. Fedorov, M. V. & Kornyshev, A. A. Ionic liquids at electrified interfaces. *Chem. Rev.* **114**, 2978–3036 (2014).
This paper offers a comprehensive overview of the theoretical understanding of the EDL structure.
44. Mezger, M. et al. Molecular layering of fluorinated ionic liquids at a charged sapphire (0001) surface. *Science* **322**, 424–428 (2008).
45. Zhou, H. et al. Nanoscale perturbations of room temperature ionic liquid structure at charged and uncharged interfaces. *ACS Nano* **6**, 9818–9827 (2012).
46. Lauw, Y. et al. Structure of [C_4mpyr][NTf_2] room-temperature ionic liquid at charged gold interfaces. *Langmuir* **28**, 7374–7381 (2012).
47. Elbourne, A. et al. Nanostructure of the ionic liquid–graphite stern layer. *ACS Nano* **9**, 7608–7620 (2015).
48. Hayes, R. et al. Double layer structure of ionic liquids at the Au(111) electrode interface: an atomic force microscopy investigation. *J. Phys. Chem. C* **115**, 6855–6863 (2011).
49. Black, J. M. et al. Bias-dependent molecular-level structure of electrical double layer in ionic liquid on graphite. *Nano Lett.* **13**, 5954–5960 (2013).
50. Li, H., Endres, F. & Atkin, R. Effect of alkyl chain length and anion species on the interfacial nanostructure of ionic liquids at the Au(111)–ionic liquid interface as a function of potential. *Phys. Chem. Chem. Phys.* **15**, 14624–14633 (2013).
51. Smith, A. M. et al. Monolayer to bilayer structural transition in confined pyrrolidinium-based ionic liquids. *J. Phys. Chem. Lett.* **4**, 378–382 (2013).
52. Fedorov, M. V., Georgi, N. & Kornyshev, A. A. Double layer in ionic liquids: the nature of the camel shape of capacitance. *Electrochem. Commun.* **12**, 296–299 (2010).
53. Tsai, W.-Y. et al. Hysteretic order-disorder transitions of ionic liquid double layer structure on graphite. *Nano Energy* **60**, 886–893 (2019).
54. Su, Y. Z., Fu, Y. C., Yan, J. W., Chen, Z. B. & Mao, B. W. Double layer of Au(100)/ionic liquid interface and its stability in imidazolium-based ionic liquids. *Angew. Chem. Int. Ed.* **48**, 5148–5151 (2009).
55. Uysal, A. et al. Interfacial ionic 'liquids': connecting static and dynamic structures. *J. Phys. Condens. Matter* **27**, 032101 (2014).
56. Black, J. M. et al. Topological defects in electric double layers of ionic liquids at carbon interfaces. *Nano Energy* **15**, 737–745 (2015).
57. Wen, R., Rahn, B. & Magnussen, O. M. Potential-dependent adlayer structure and dynamics at the ionic liquid/Au(111) interface: a molecular-scale in situ video-STM study. *Angew. Chem. Int. Ed.* **54**, 6062–6066 (2015).
58. Kirchner, K., Kirchner, T., Ivaništšev, V. & Fedorov, M. V. Electrical double layer in ionic liquids: structural transitions from multilayer to monolayer structure at the interface. *Electrochim. Acta* **110**, 762–771 (2013).
59. Ivaništšev, V. & Fedorov, M. V. Interfaces between charged surfaces and ionic liquids: insights from molecular simulations. *Electrochem. Soc. Interface* **23**, 65–69 (2014).
60. Chu, M., Miller, M. & Dutta, P. Crowding and anomalous capacitance at an electrode–ionic liquid interface observed using operando X-ray scattering. *ACS Cent. Sci.* **2**, 175–180 (2016).
61. Nishi, N. et al. Potential-dependent structure of the ionic layer at the electrode interface of an ionic liquid probed using neutron reflectometry. *J. Phys. Chem. C* **123**, 9223–9230 (2019).
62. Beltrop, K. et al. Does size really matter? New insights into the intercalation behavior of anions into a graphite-based positive electrode for dual-ion batteries. *Electrochim. Acta* **209**, 44–55 (2016).
63. Rodrigues, M.-T. F. et al. A materials perspective on Li-ion batteries at extreme temperatures. *Nat. Energy* **2**, 17108 (2017).
64. Umebayashi, Y. et al. Raman spectroscopic studies and ab initio calculations on conformational isomerism of 1-butyl-3-methylimidazolium bis-(trifluoromethanesulfonyl)amide solvated to a lithium ion in ionic liquids: effects of the second solvation sphere of the lithium ion. *J. Phys. Chem. B* **114**, 6513–6521 (2010).
65. Ishihara, Y., Miyazaki, K., Fukutsuka, T. & Abe, T. Lithium-ion transfer at the interface between high potential negative electrodes and ionic liquids. *J. Electrochem. Soc.* **161**, A1939–A1942 (2014).
66. Matsumoto, H., Sakaebe, H. & Tatsumi, K. Li/$LiCoO_2$ cell performance using ionic liquids composed of N,N-diethyl-N-methyl-N-(2-methoxyethyl)ammonium-effect of anionic structure. *ECS Trans.* **16**, 59–66 (2009).
67. Ishikawa, M., Sugimoto, T., Kikuta, M., Ishiko, E. & Kono, M. Pure ionic liquid electrolytes compatible with a graphitized carbon negative electrode in rechargeable lithium-ion batteries. *J. Power Sources* **162**, 658–662 (2006).
68. Balducci, A. et al. Ionic liquids as electrolyte in lithium batteries: in situ FTIRs studies on the use of electrolyte additives. *ECS Trans.* **11**, 109–114 (2008).
69. Mun, J. et al. Electrochemical stability of bis(trifluoromethanesulfonyl)imide-based ionic liquids at elevated temperature as a solvent for a titanium oxide bronze electrode. *J. Power Sources* **194**, 1068–1074 (2009).
70. Garcia, B., Lavallée, S., Perron, G., Michot, C. & Armand, M. Room temperature molten salts as lithium battery electrolyte. *Electrochim. Acta* **49**, 4583–4588 (2004).
71. Sakaebe, H. & Matsumoto, H. *N*-Methyl-*N*-propylpiperidinium bis(trifluoromethanesulfonyl)imide (PP13–TFSI)-novel electrolyte base for Li battery. *Electrochem. Commun.* **5**, 594–598 (2003).
72. Lu, W. et al. An in-situ Raman spectroscopic study on the cathodic process of EMITFSI ionic liquid on Ag electrodes. *J. Electroanal. Chem.* **819**, 435–441 (2018).
73. Xiao, L. & Johnson, K. E. Electrochemistry of 1-butyl-3-methyl-1H-imidazolium tetrafluoroborate ionic liquid. *J. Electrochem. Soc.* **150**, E307–E311 (2003).
74. Seki, S. et al. Lithium secondary batteries using modified-imidazolium room-temperature ionic liquid. *J. Phys. Chem. B* **110**, 10228–10230 (2006).

75. Fernicola, A., Croce, F., Scrosati, B., Watanabe, T. & Ohno, H. LiTFSI-BEPyTFSI as an improved ionic liquid electrolyte for rechargeable lithium batteries. *J. Power Sources* **174**, 342–348 (2007).
76. Girard, G. et al. Electrochemical and physicochemical properties of small phosphonium cation ionic liquid electrolytes with high lithium salt content. *Phys. Chem. Chem. Phys.* **17**, 8706–8713 (2015).
77. Seki, S. et al. Effects of alkyl chain in imidazolium-type room-temperature ionic liquids as lithium secondary battery electrolytes. *Electrochem. Solid-State Lett.* **10**, A237–A240 (2007).
78. Lian, C., Liu, H. & Wu, J. Ionic liquid mixture expands the potential window and capacitance of a supercapacitor in tandem. *J. Phys. Chem. C* **122**, 18304–18310 (2018).
79. Lin, D., Liu, Y. & Cui, Y. Reviving the lithium metal anode for high-energy batteries. *Nat. Nanotechnol.* **12**, 194–206 (2017).
80. Cheng, X.-B., Zhang, R., Zhao, C.-Z. & Zhang, Q. Toward safe lithium metal anode in rechargeable batteries: a review. *Chem. Rev.* **117**, 10403–10473 (2017).
81. Cheng, X.-B. et al. Nanodiamonds suppress the growth of lithium dendrites. *Nat. Commun.* **8**, 336 (2017).
82. Akolkar, R. Modeling dendrite growth during lithium electrodeposition at sub-ambient temperature. *J. Power Sources* **246**, 84–89 (2014).
83. Grande, L. et al. Homogeneous lithium electrodeposition with pyrrolidinium-based ionic liquid electrolytes. *ACS Appl. Mater. Interfaces* **7**, 5950–5958 (2015).
84. Yildirim, H., Haskins, J. B., Bauschlicher, C. W. Jr & Lawson, J. W. Decomposition of ionic liquids at lithium interfaces. 1. *Ab initio* molecular dynamics simulations. *J. Phys. Chem. C* **121**, 28214–28234 (2017).
85. Merinov, B. V. et al. Interface structure in Li-metal/$[Pyr_{14}][TFSI]$-ionic liquid system from ab initio molecular dynamics simulations. *J. Phys. Chem. Lett.* **10**, 4577–4586 (2019).
86. Xu, K. & von Wald Cresce, A. Li^+-solvation/desolvation dictates interphasial processes on graphitic anode in Li ion cells. *J. Mater. Res.* **27**, 2327–2341 (2012).
87. Wu, Y. et al. A room-temperature liquid metal-based self-healing anode for lithium-ion batteries with an ultra-long cycle life. *Energy Environ. Sci.* **10**,1854–1861 (2017).
88. Ye, H. et al. Stable Li plating/stripping electrochemistry realized by a hybrid Li reservoir in spherical carbon granules with 3D conducting skeletons. *J. Am. Chem. Soc.* **139**, 5916–5922 (2017).
89. Zheng, G. et al. Interconnected hollow carbon nanospheres for stable lithium metal anodes. *Nat. Nanotechnol.* **9**, 618–623 (2014).
90. Li, N. et al. Suppressing dendritic lithium formation using porous media in lithium metal-based batteries. *Nano Lett.* **18**, 2067–2073 (2018).
91. Rothermel, S. et al. Dual-graphite cells based on the reversible intercalation of bis(trifluoromethanesulfonyl) imide anions from an ionic liquid electrolyte. *Energy Environ. Sci.* **7**, 3412–3423 (2014).
92. An, S. J. et al. The state of understanding of the lithium-ion-battery graphite solid electrolyte interphase (SEI) and its relationship to formation cycling. *Carbon* **105**, 52–76 (2016).
93. Achiha, T. et al. Thermal stability and electrochemical properties of fluorine compounds as nonflammable solvents for lithium-ion batteries. *J. Electrochem. Soc.* **157**, A707–A712 (2010).
94. Tan, S., Ji, Y. J., Zhang, Z. R. & Yang, Y. Recent progress in research on high-voltage electrolytes for lithium-ion batteries. *ChemPhysChem* **15**, 1956–1969 (2014).
95. Peljo, P. & Girault, H. Electrochemical potential window of battery electrolytes: the HOMO–LUMO misconception. *Energy Environ. Sci.* **11**, 2306–2309 (2018).
96. Tsuda, T. et al. Design, synthesis, and electrochemistry of room-temperature ionic liquids functionalized with propylene carbonate. *Angew. Chem. Int. Ed.* **50**, 1310–1313 (2011).
97. Li, Y. et al. A novel electrolyte salt additive for lithium-ion batteries with voltages greater than 4.7 V. *Adv. Energy Mater.* **7**, 1601397 (2017).
98. Wang, Y. et al. Accelerating rate calorimetry studies of the reactions between ionic liquids and charged lithium ion battery electrode materials. *Electrochim. Acta* **52**, 6346–6352 (2007).
99. Waldmann, T., Wilka, M., Kasper, M., Fleischhammer, M. & Wohlfahrt-Mehrens, M. Temperature dependent ageing mechanisms in lithium-ion batteries–a post-mortem study. *J. Power Sources* **262**, 129–135 (2014).
100. Markevich, E. et al. High performance of thick amorphous columnar monolithic film silicon anodes in ionic liquid electrolytes at elevated temperature. *RSC Adv.* **4**, 48572–48575 (2014).
101. Ababtain, K. et al. Ionic liquid–organic carbonate electrolyte blends to stabilize silicon electrodes for extending lithium ion battery operability to 100°C. *ACS Appl. Mater. Interfaces* **8**, 15242–15249 (2016).
102. Rodrigues, M.-T. F., Sayed, F. N., Gullapalli, H. & Ajayan, P. M. High-temperature solid electrolyte interphases (SEI) in graphite electrodes. *J. Power Sources* **381**, 107–115 (2018).
103. Kerr, R. et al. High-capacity retention of Si anodes using a mixed lithium/phosphonium bis(fluorosulfonyl) imide ionic liquid electrolyte. *ACS Energy Lett.* **2**, 1804–1809 (2017).
104. Munoz-Rojas, D. et al. Development and implementation of a high temperature electrochemical cell for lithium batteries. *Electrochem. Commun.* **9**, 708–712 (2007).
105. Rodrigues, M. T. F. et al. Hexagonal boron nitride-based electrolyte composite for Li-ion battery operation from room temperature to 150°C. *Adv. Energy Mater.* **6**, 1600218 (2016).
106. Borges, R. S. et al. Supercapacitor operating at 200 degrees celsius. *Sci. Rep.* **3**, 2572 (2013).
107. Gowda, S. R. et al. Three-dimensionally engineered porous silicon electrodes for Li ion batteries. *Nano Lett.* **12**, 6060–6065 (2012).
108. Weingärtner, H. Understanding ionic liquids at the molecular level: facts, problems, and controversies. *Angew. Chem. Int. Ed.* **47**, 654–670 (2008).
109. Angell, C. A., Ansari, Y. & Zhao, Z. Ionic liquids: past, present and future. *Faraday Discuss.* **154**, 9–27 (2012).
110. Böckenfeld, N., Willeke, M., Pires, J., Anouti, M. & Balducci, A. On the use of lithium iron phosphate in combination with protic ionic liquid-based electrolytes. *J. Electrochem. Soc.* **160**, A559–A563 (2013).
111. Menne, S., Pires, J., Anouti, M. & Balducci, A. Protic ionic liquids as electrolytes for lithium-ion batteries. *Electrochem. Commun.* **31**, 39–41 (2013).
112. Vogl, T., Menne, S., Kühnel, R.-S. & Balducci, A. The beneficial effect of protic ionic liquids on the lithium environment in electrolytes for battery applications. *J. Mater. Chem. A* **2**, 8258–8265 (2014).
113. Yamada, Y. & Yamada, A. Superconcentrated electrolytes for lithium batteries. *J. Electrochem. Soc.* **162**, A2406–A2423 (2015).
114. Wang, J. et al. Superconcentrated electrolytes for a high-voltage lithium-ion battery. *Nat. Commun.* **7**, 12032 (2016).
115. Menne, S., Vogl, T. & Balducci, A. Lithium coordination in protic ionic liquids. *Phys. Chem. Chem. Phys.* **16**, 5485–5489 (2014).
116. Vogl, T., Menne, S. & Balducci, A. Mixtures of protic ionic liquids and propylene carbonate as advanced electrolytes for lithium-ion batteries. *Phys. Chem. Chem. Phys.* **16**, 25014–25023 (2014).
117. Wang, J. et al. Fire-extinguishing organic electrolytes for safe batteries. *Nat. Energy* **3**, 22–29 (2018).
118. Ueno, K. et al. Glyme–lithium salt equimolar molten mixtures: concentrated solutions or solvate ionic liquids? *J. Phys. Chem. B* **116**, 11323–11331 (2012).
119. Ueno, K. et al. Li^+ solvation in glyme–Li salt solvate ionic liquids. *Phys. Chem. Chem. Phys.* **17**, 8248–8257 (2015).
120. Saito, S. et al. Li^+ local structure in hydrofluoroether diluted Li-glyme solvate ionic liquid. *J. Phys. Chem. B* **120**, 3378–3387 (2016).
121. Gorska, B., Frackowiak, E. & Beguin, F. Redox active electrolytes in carbon/carbon electrochemical capacitors. *Curr. Opin. Electrochem.* **9**, 95–105 (2018).
122. Armand, M. & Tarascon, J.-M. Building better batteries. *Nature* **451**, 652–657 (2008).
123. Appetecchi, G. B., Kim, G.-T., Montanino, M., Alessandrini, F. & Passerini, S. Room temperature lithium polymer batteries based on ionic liquids. *J. Power Sources* **196**, 6703–6709 (2011).
124. Ma, Q. et al. Single lithium-ion conducting polymer electrolytes based on a super-delocalized polyanion. *Angew. Chem. Int. Ed.* **55**, 2521–2525 (2016).
125. Li, X., Zhang, Z., Li, S., Yang, L. & Hirano, S.-I. Polymeric ionic liquid-plastic crystal composite electrolytes for lithium ion batteries. *J. Power Sources* **307**, 678–683 (2016).
126. Safa, M., Chamaani, A., Chawla, N. & El-Zahab, B. Polymeric ionic liquid gel electrolyte for room temperature lithium battery applications. *Electrochim. Acta* **213**, 587–593 (2016).
127. Kelly, J. C., Degrood, N. L. & Roberts, M. E. Li-ion battery shut-off at high temperature caused by polymer phase separation in responsive electrolytes. *Chem. Commun.* **51**, 5448–5451 (2015).
128. Marczewski, M. J., Stanje, B., Hanzu, I., Wilkening, M. & Johansson, P. "Ionic liquids-in-salt"-a promising electrolyte concept for high-temperature lithium batteries? *Phys. Chem. Chem. Phys.* **16**, 12341–12349 (2014).
129. Janssen, P. et al. Shutdown potential adjustment of modified carbene adducts as additives for lithium ion battery electrolytes. *J. Power Sources* **367**, 72–79 (2017).
130. Streipert, B. et al. Evaluation of allylboronic acid pinacol ester as effective shutdown overcharge additive for lithium ion cells. *J. Electrochem. Soc.* **164**, A168–A172 (2016).
131. Chen, Z. et al. Fast and reversible thermoresponsive polymer switching materials for safer batteries. *Nat. Energy* **1**, 15009 (2016).
132. Eftekharnia, M., Hasanpoor, M., Forsyth, M., Kerr, R. & Howlett, P. C. Toward practical Li metal batteries: importance of separator compatibility using ionic liquid electrolytes. *ACS Appl. Energy Mater.* **2**, 6655–6663 (2019).
133. Lee, H., Yanilmaz, M., Toprakci, O., Fu, K. & Zhang, X. A review of recent developments in membrane separators for rechargeable lithium-ion batteries. *Energy Environ. Sci.* **7**, 3857–3886 (2014).
134. Kalaga, K. et al. Quasi-solid electrolytes for high temperature lithium ion batteries. *ACS Appl. Mater. Interfaces* **7**, 25777–25783 (2015).
135. Wu, F. et al. Novel solid-state Li/$LiFePO_4$ battery configuration with a ternary nanocomposite electrolyte for practical applications. *Adv. Mater.* **23**, 5081–5085 (2011).
136. Zhan, C., Zhang, Y., Cummings, P. T. & Jiang, D.-E. Computational insight into the capacitive performance of graphene edge planes. *Carbon* **116**, 278–285 (2017).
137. Dyatkin, B. et al. Influence of surface oxidation on ion dynamics and capacitance in porous and nonporous carbon electrodes. *J. Phys. Chem. C* **120**, 8730–8741 (2016).
138. Dyatkin, B. et al. Ionic liquid structure, dynamics, and electrosorption in carbon electrodes with bimodal pores and heterogeneous surfaces. *Carbon* **129**, 104–118 (2018).
139. Kerisit, S., Schwenzer, B. & Vijayakumar, M. Effects of oxygen-containing functional groups on supercapacitor performance. *J. Phys. Chem. Lett.* **5**, 2330–2334 (2014).
140. Zhang, Y., Dyatkin, B. & Cummings, P. T. Molecular investigation of oxidized graphene: anatomy of the double-layer structure and ion dynamics. *J. Phys. Chem. C* **123**, 12583–12591 (2019).
141. Chmiola, J. et al. Anomalous increase in carbon capacitance at pore sizes less than 1 nanometer. *Science* **313**, 1760–1763 (2006).
142. Celine, L. et al. Relation between the ion size and pore size for an electric double-layer capacitor. *J. Am. Chem. Soc.* **130**, 2730–2731 (2008).
143. Jiang, D.-e., Jin, Z. & Wu, J. Oscillation of capacitance inside nanopores. *Nano Lett.* **11**, 5373–5377 (2011).
144. Feng, G. & Cummings, P. T. Supercapacitor capacitance exhibits oscillatory behavior as a function of nanopore size. *J. Phys. Chem. Lett.* **2**, 2859–2864 (2011).
145. Wu, P., Huang, J., Meunier, V., Sumpter, B. G. & Qiao, R. Complex capacitance scaling in ionic liquids-filled nanopores. *ACS Nano* **5**, 9044–9051 (2011).
146. Jiang, D.-e., Jin, Z., Henderson, D. & Wu, J. Solvent effect on the pore-size dependence of an organic electrolyte supercapacitor. *J. Phys. Chem. Lett.* **3**, 1727–1731 (2012).
147. Wang, X. et al. Geometrically confined favourable ion packing for high gravimetric capacitance in carbon–ionic liquid supercapacitors. *Energy Environ. Sci.* **9**, 232–239 (2016).
148. Kondrat, S., Perez, C., Presser, V., Gogotsi, Y. & Kornyshev, A. Effect of pore size and its dispersity on the energy storage in nanoporous supercapacitors. *Energy Environ. Sci.* **5**, 6474–6479 (2012).
149. Vasilyev, O. A., Kornyshev, A. A. & Kondrat, S. Connections matter: on the importance of pore percolation for nanoporous supercapacitors. *ACS Appl. Energy Mater.* **2**, 5386–5390 (2019).
150. Drüschler, M. et al. New insights into the interface between a single-crystalline metal electrode and an extremely pure ionic liquid: slow interfacial processes

and the influence of temperature on interfacial dynamics. *Phys. Chem. Chem. Phys.* **14**, 5090–5099 (2012).

151. Wang, H. et al. Real-time NMR studies of electrochemical double-layer capacitors. *J. Am. Chem. Soc.* **133**, 19270–19273 (2011).
152. McDonough, J. K. et al. Influence of the structure of carbon onions on their electrochemical performance in supercapacitor electrodes. *Carbon* **50**, 3298–3309 (2012).
153. Chu, M., Miller, M., Douglas, T. & Dutta, P. Ultraslow dynamics at a charged silicon–ionic liquid interface revealed by X-ray reflectivity. *J. Phys. Chem. C* **121**, 3841–3845 (2017).
154. He, Y. et al. Importance of ion packing on the dynamics of ionic liquids during micropore charging. *J. Phys. Chem. Lett.* **7**, 36–42 (2016).
155. Dyatkin, B. et al. High capacitance of coarse-grained carbide derived carbon electrodes. *J. Power Sources* **306**, 32–41 (2016).
156. Lian, C., Su, H., Li, C., Liu, H. & Wu, J. Nonnegligible roles of pore size distribution on electroosmotic flow in nanoporous materials. *ACS Nano* **13**, 8185–8192 (2019).
157. Liu, L. et al. Capacitance of coarse-grained carbon electrodes with thickness up to 800 μm. *Electrochim. Acta* **302**, 38–44 (2019).
158. Forse, A. C. et al. Direct observation of ion dynamics in supercapacitor electrodes using in situ diffusion NMR spectroscopy. *Nat. Energy* **2**, 16216 (2017).
This study uses in situ NMR to reveal the factors that influence ion diffusion in porous carbon.
159. Richey, F. W., Dyatkin, B., Gogotsi, Y. & Elabd, Y. A. Ion dynamics in porous carbon electrodes in supercapacitors using in situ infrared spectroelectrochemistry. *J. Am. Chem. Soc.* **135**, 12818–12826 (2013).
160. Forse, A. C., Merlet, C., Griffin, J. M. & Grey, C. P. New perspectives on the charging mechanisms of supercapacitors. *J. Am. Chem. Soc.* **138**, 5731–5744 (2016).
161. Griffin, J. M. et al. In situ NMR and electrochemical quartz crystal microbalance techniques reveal the structure of the electrical double layer in supercapacitors. *Nat. Mater.* **14**, 812–819 (2015).
162. Forse, A. C. et al. NMR study of ion dynamics and charge storage in ionic liquid supercapacitors. *J. Am. Chem. Soc.* **137**, 7231–7242 (2015).
163. Tsai, W.-Y., Taberna, P.-L. & Simon, P. Electrochemical quartz crystal microbalance (EQCM) study of ion dynamics in nanoporous carbons. *J. Am. Chem. Soc.* **136**, 8722–8728 (2014).
164. Merlet, C. et al. On the molecular origin of supercapacitance in nanoporous carbon electrodes. *Nat. Mater.* **11**, 306–310 (2012).
165. Merlet, C., Forse, A. C., Griffin, J. M., Frenkel, D. & Grey, C. P. Lattice simulation method to model diffusion and NMR spectra in porous materials. *J. Chem. Phys.* **142**, 094701 (2015).
166. Bañuelos, J. L. et al. The influence of a hierarchical porous carbon network on the coherent dynamics of a nanoconfined room temperature ionic liquid: a neutron spin echo and atomistic simulation investigation. *Carbon* **78**, 415–427 (2014).
167. Boukhalfa, S. et al. In situ small angle neutron scattering revealing ion sorption in microporous carbon electrical double layer capacitors. *ACS Nano* **8**, 2495–2503 (2014).
168. Bañuelos, J. L. et al. Densification of ionic liquid molecules within a hierarchical nanoporous carbon structure revealed by small-angle scattering and molecular dynamics simulation. *Chem. Mater.* **26**, 1144–1153 (2013).
169. Kondrat, S. & Kornyshev, A. A. Pressing a spring: what does it take to maximize the energy storage in nanoporous supercapacitors? *Nanoscale Horiz.* **1**, 45–52 (2016).
170. Lee, A. A., Kondrat, S. & Kornyshev, A. A. Single-file charge storage in conducting nanopores. *Phys. Rev. Lett.* **113**, 048701 (2014).
171. Kondrat, S., Wu, P., Qiao, R. & Kornyshev, A. A. Accelerating charging dynamics in subnanometre pores. *Nat. Mater.* **13**, 387–393 (2014).
172. Kondrat, S. & Kornyshev, A. Charging dynamics and optimization of nanoporous supercapacitors. *J. Phys. Chem. C* **117**, 12399–12406 (2013).
173. Kondrat, S. & Kornyshev, A. Superionic state in double-layer capacitors with nanoporous electrodes. *J. Phys. Condens. Matter* **23**, 022201 (2010).
174. Kiyohara, K. & Asaka, K. Monte Carlo simulation of electrolytes in the constant voltage ensemble. *J. Chem. Phys.* **126**, 214704 (2007).
175. Jiang, D.-e. & Wu, J. Microscopic insights into the electrochemical behavior of nonaqueous electrolytes in electric double-layer capacitors. *J. Phys. Chem. Lett.* **4**, 1260–1267 (2013).
176. He, Y., Huang, J., Sumpter, B. G., Kornyshev, A. A. & Qiao, R. Dynamic charge storage in ionic liquids-filled nanopores: insight from a computational cyclic voltammetry study. *J. Phys. Chem. Lett.* **6**, 22–30 (2014).
177. Pak, A. J. & Hwang, G. S. Charging rate dependence of ion migration and stagnation in ionic- liquid-filled carbon nanopores. *J. Phys. Chem. C* **120**, 24560–24567 (2016).
178. Kornyshev, A. A. The simplest model of charge storage in single file metallic nanopores. *Faraday Discuss.* **164**, 117–133 (2013).
179. Zhang, S., Xu, K. & Jow, T. Electrochemical impedance study on the low temperature of Li-ion batteries. *Electrochim. Acta* **49**, 1057–1061 (2004).
180. Balabajew, M., Kranz, T. & Roling, B. Ion-transport processes in dual-ion cells utilizing a $Pyr_{1,4}$TFSI/LiTFSI mixture as the electrolyte. *ChemElectroChem* **2**, 1991–2000 (2015).
181. Fan, J. & Tan, S. Studies on charging lithium-ion cells at low temperatures. *J. Electrochem. Soc.* **153**, A1081–A1092 (2006).
182. Kim, T., Jung, G., Yoo, S., Suh, K. S. & Ruoff, R. S. Activated graphene-based carbons as supercapacitor electrodes with macro- and mesopores. *ACS Nano* **7**, 6899–6905 (2013).
183. Yan, R., Antonietti, M. & Oschatz, M. Toward the experimental understanding of the energy storage mechanism and ion dynamics in ionic liquid based supercapacitors. *Adv. Energy Mater.* **8**, 1800026 (2018).
184. Zhao, M. Q. et al. Flexible MXene/carbon nanotube composite paper with high volumetric capacitance. *Adv. Mater.* **27**, 339–345 (2015).
185. Xie, X. et al. Porous heterostructured MXene/carbon nanotube composite paper with high volumetric capacity for sodium-based energy storage devices. *Nano Energy* **26**, 513–523 (2016).
186. Boota, M. et al. Pseudocapacitive electrodes produced by oxidant-free polymerization of pyrrole between the layers of 2D titanium carbide (MXene). *Adv. Mater.* **28**, 1517–1522 (2016).
187. Zhao, M.-Q. et al. 2D titanium carbide and transition metal oxides hybrid electrodes for Li-ion storage. *Nano Energy* **30**, 603–613 (2016).
188. Luo, J. et al. Pillared structure design of MXene with ultralarge interlayer spacing for high- performance lithium-ion capacitors. *ACS Nano* **11**, 2459–2469 (2017).
189. Xia, Y. et al. Thickness-independent capacitance of vertically aligned liquid-crystalline MXenes. *Nature* **557**, 409–412 (2018).
This study reports the design of a vertically aligned structure that allows fast ion diffusion almost independent of the electrode thickness.
190. Tsai, W.-Y. et al. Outstanding performance of activated graphene based supercapacitors in ionic liquid electrolyte from -50 to 80 °C. *Nano Energy* **2**, 403–411 (2013).
191. Futamura, R. et al. Partial breaking of the Coulombic ordering of ionic liquids confined in carbon nanopores. *Nat. Mater.* **16**, 1225–1232 (2017).
This study reports that, under nanoconfinement, like-charged ion pairs are formed.
192. Kondrat, S., Georgi, N., Fedorov, M. V. & Kornyshev, A. A. A superionic state in nano-porous double-layer capacitors: insights from Monte Carlo simulations. *Phys. Chem. Chem. Phys.* **13**, 11359–11366 (2011).
193. Kong, J. et al. Temperature dependence of ion diffusion coefficients in NaCl electrolyte confined within graphene nanochannels. *Phys. Chem. Chem. Phys.* **19**, 7678–7688 (2017).
194. Zhang, Y. & Cummings, P. T. Effects of solvent concentration on the performance of ionic-liquid/ carbon supercapacitors. *ACS Appl. Mater. Interfaces* **11**, 42680–42689 (2019).
195. Burt, R. et al. Capacitance of nanoporous carbon-based supercapacitors is a trade-off between the concentration and the separability of the ions. *J. Phys. Chem. Lett.* **7**, 4015–4021 (2016).
196. Wang, X. et al. Unimpeded migration of ions in carbon electrodes with bimodal pores at an ultralow temperature of -100 °C. *J. Mater. Chem. A* **7**, 16339–16346 (2019).
197. Esfandiar, A. et al. Size effect in ion transport through angstrom-scale slits. *Science* **358**, 511–513 (2017).
198. Merlet, C. et al. Highly confined ions store charge more efficiently in supercapacitors. *Nat. Commun.* **4**, 2701 (2013).
199. Prehal, C. et al. Quantification of ion confinement and desolvation in nanoporous carbon supercapacitors with modelling and in situ X-ray scattering. *Nat. Energy* **2**, 16215 (2017).
200. Surwade, S. P. et al. Electrochemical control of ion transport through a mesoporous carbon membrane. *Langmuir* **30**, 3606–3611 (2014).
201. Banda, H. et al. Ion sieving effects in chemically tuned pillared graphene materials for electrochemical capacitors. *Chem. Mater.* **30**, 3040–3047 (2018).
202. Wang, X. et al. Selective charging behavior in an ionic mixture electrolyte–supercapacitor system for higher energy and power. *J. Am. Chem. Soc.* **139**, 18681–18687 (2017).
203. Doherty, A. P. Redox-active ionic liquids for energy harvesting and storage applications. *Curr. Opin. Electrochem.* **7**, 61–65 (2018).
204. Mourad, E. et al. Biredox ionic liquids with solid-like redox density in the liquid state for high-energy supercapacitors. *Nat. Mater.* **16**, 446–453 (2017).
This study reports the design of ionic liquids with both redox-active cations and anions for greatly enhanced capacitance in carbon materials.
205. Matsumoto, M. et al. Exceptionally high electric double layer capacitances of oligomeric ionic liquids. *J. Am. Chem. Soc.* **139**, 16072–16075 (2017).
206. Mao, X. et al. Self-assembled nanostructures in ionic liquids facilitate charge storage at electrified interfaces. *Nat. Mater.* **18**, 1350–1357 (2019).
207. Suo, L. et al. "Water-in-salt" electrolyte enables high-voltage aqueous lithium-ion chemistries. *Science* **350**, 938–943 (2015).
This study reports the advantages of using a 'water-in-salt' electrolyte in Li-ion batteries; the same strategy could be applied to design a 'solvent-in-ionic-liquid' electrolyte.
208. Acerce, M., Voiry, D. & Chhowalla, M. Metallic 1T phase MoS_2 nanosheets as supercapacitor electrode materials. *Nat. Nanotechnol.* **10**, 313–318 (2015).
209. Lukatskaya, M. R. et al. Ultra-high-rate pseudocapacitive energy storage in two-dimensional transition metal carbides. *Nat. Energy* **2**, 17105 (2017).
210. Lin, Z. et al. Capacitance of $Ti_3C_2T_x$ MXene in ionic liquid electrolyte. *J. Power Sources* **326**, 575–579 (2016).
211. Pomerantseva, E. & Gogotsi, Y. Two-dimensional heterostructures for energy storage. *Nat. Energy* **2**, 17089 (2017).
212. Wang, X. et al. Influences from solvents on charge storage in titanium carbide MXenes. *Nat. Energy* **4**, 241–248 (2019).
This study reports that the choice of solvent has a strong impact on the charge-storage capability and ion transport in 2D MXenes, demonstrating the importance of matching the electrolyte to the electrode material.
213. Griffin, J. et al. Ion counting in supercapacitor electrodes using NMR spectroscopy. *Faraday Discuss.* **176**, 49–68 (2014).